Computational Characterization of Noise in Nonlinear Nanomechanical Resonators

by

Fiona Polloshka

A Thesis Submitted to the
Graduate School of Sciences and Engineering
in Partial Fulfillment of the Requirements for
the Degree of

Master of Science

in

Electrical and Electronics Engineering

KOÇ ÜNİVERSİTESİ

September 8, 2021

Computational Characterization of Noise in Nonlinear Nanomechanical Resonators

Koç University

Graduate School of Sciences and Engineering

This is to certify that I have examined this copy of a master's thesis by

Fiona Polloshka

and have found that it is complete and satisfactory in all respects,

and that any and all revisions required by the final

examining committee have been made.

Committee Members:

Prof. Alper Demir (Advisor)

Assist. Prof. Mehmet Selim Hanay

Assist. Prof. Önder Şuvak

Date:

Për nanën dhe babën

To mom and dad

ABSTRACT

Computational Characterization of Noise in
Nonlinear Nanomechanical Resonators
Fiona Polloshka
Master of Science in Electrical and Electronics Engineering
September 8, 2021

Recent breakthroughs in nanotechnology have paved the way for huge advances in the field of nano-electro-mechanical systems (NEMS). Nanomechanical resonators are used as accurate mass and force sensors in mass spectrometry and atomic force microscopy. In most current sensing schemes, the resonators operate in the linear regime, where changes in mass and force are detected by tracking the shifts in the resonance frequency. The use of resonators operating in the nonlinear regime has been recently proposed due to shrinking device sizes and some claimed advantages over linear operation. As with linear resonators, the sensor performance is ultimately limited by the inherent frequency fluctuations arising from various sources of noise. However, due to nonlinear behavior, device dynamics is intricate and noise characterization is more challenging. The fundamental sensitivity limits of resonant sensors operating in the nonlinear regime need to be determined quantitatively in order to examine their performance and assess their pros and cons over linear resonators. In this thesis, we present an efficient computational technique for characterizing the frequency fluctuations in nonlinear Duffing resonators due to noise. The method is based on repurposing and adapting a non Monte Carlo stochastic analysis technique that was originally developed for noise analysis of analog electronic circuits. The proposed technique presents the capability for noise characterization under various dynamic sensing schemes, e.g., when drive frequency is time-varying and continually updated in a closed-loop setup. We compare the results obtained with the proposed technique against extensive, carefully run Monte Carlo simulations and demonstrate that the same accuracy can be achieved with drastically reduced computation time and in a more robust manner. We furthermore compare the results of our proposed method with experimental open-loop sweep characterizations reported in the literature. We analyze the open-loop sweep method and highlight its shortcomings

as a sensing scheme. Finally, we compare the noise performance in the linear and nonlinear operating regimes, and discuss the advantages of using one over the other.

ÖZETÇE

Doğrusal Olmayan Nanomekanik Rezonatörlerde Gürültünün Hesaplamalı Karakterizasyonu
Fiona Polloshka
Elektrik ve Elektronik Mühendisliği, Yüksek Lisans
8 Eylül 2021

Nanoteknolojideki son atılımlar, nano-elektro-mekanik sistemler (NEMS) alanında önemli ilerlemelerin yolunu açmıştır. Nanomekanik rezonatörler, kütle spektrometrisi ve atomik kuvvet mikroskobu uygulamalarında hassasiyeti yüksek kütle ve kuvvet sensörleri olarak kullanılmaktadır. Mevcut sensör mimarilerinin çoğunda, rezonatörler, rezonans frekansındaki kaymaları izleyerek kütle ve kuvvetteki değişikliklerin tespit edildiği doğrusal rejimde çalışırlar. Doğrusal olmayan rejimde çalışan rezonatörlerin kullanımı, küçülen cihaz boyutları ve doğrusal operasyona nispeten bazı avantajlar nedeniyle yakın zaman önce önerilmiştir. Doğrusal rezonatörlerde olduğu gibi, sensör performansı nihayetinde gürültüden kaynaklanan frekans dalgalanmaları ile belirlenir. Ancak doğrusal olmayan davranış nedeniyle cihaz dinamikleri karmaşıktır ve gürültü karakterizasyonu daha zordur. Doğrusal olmayan rejimde çalışan rezonans bazlı sensörlerin temel hassasiyet sınırlarını, performanslarını ve doğrusal rezonatörlere göre artılarını ve eksilerini değerlendirmek için ayrıntılı bir karakterizasyonun yapılması gerekmektedir. Bu tezde, doğrusal olmayan Duffing rezonatörlerinde gürültü nedeniyle frekans dalgalanmalarını karakterize etmek için verimli bir hesaplama yöntemi sunulmaktadır. Yöntem, orijinal olarak analog elektronik devrelerin gürültü analizi için geliştirilmiş Monte Carlo bazlı olmayan bir stokastik analiz yönteminin uyarlamasına dayanmaktadır. Önerilen yöntem, çeşitli dinamik sensör mimarileri için, örneğin sürücü frekansı zamana göre değiştiğinde ve bir kapalı döngü kurulumunda sürekli olarak güncellendiğinde, gürültü karakterizasyonunu mümkün kılar. Önerilen yöntemle elde edilen sonuçlar, kapsamlı ve dikkatli bir şekilde koşturulmuş Monte Carlo simülasyonlarıyla karşılaştırılmakta ve aynı sonuçların büyük ölçüde azaltılmış hesaplama süresi ile ve daha güvenilir bir şekilde elde edilebileceği gösterilmektedir. Ayrıca, önerilen yöntemle elde edilen sonuçlar literatürdeki deneysel açık döngü tarama karakterizasyonları ile karşılaştırılmaktadır.

Açık döngü tarama yönteminin ayrıntılı bir analizi yapılmakta ve bir sensör yöntemi olarak eksiklikleri vurgulanmaktadır. Son olarak, doğrusal ve doğrusal olmayan çalışma rejimlerindeki gürültü performansı karşılaştırılmaktadır.

ACKNOWLEDGMENTS

I would like to express my deepest gratitude to my advisor Prof. Alper Demir for his invaluable guidance, encouragement, and patience throughout this study. His exceptional insight and our many discussions have contributed immensely to this thesis project. I would also like to thank my mentor Prof. Alper Erdogan, who contributed greatly to my growth as a person and a researcher. I feel tremendously lucky to have had such excellent role models to look up to throughout my graduate experience. They set a very high standard that I hope to live up to one day.

I would like to express my sincere thanks to Assist. Prof. Mehmet Selim Hanay and Assist. Prof. Önder Şuvak for taking part in my thesis committee and contributing with valuable comments and suggestions.

I would also like to thank my friends Merve, Gökcan, Onur, and Farzin for their friendship, late nights, fruitful discussions, and creating an inspiring research environment.

I want to wholeheartedly thank all my friends from Lelz for opening their hearts and homes to me during these challenging times, and for being my family away from home.

Last, but not least, I would like to thank my family for their love and unwavering support. I am forever indebted to my parents, who have sacrificed a lot for me to be where I am today and have supported me every step of the way. I want to thank my sister Bleta for always being there for me when I needed her most. I thank Aurora and Vullnet for being a constant source of joy in my life. I feel very lucky to have them.

TABLE OF CONTENTS

List of Figures **xi**

Abbreviations **xv**

Chapter 1: Background **1**

1.1 Introduction 1

1.2 Oscillatory Systems 4

1.2.1 Linear Oscillations 4

1.2.2 Nonlinear Oscillations 5

Chapter 2: Theory **9**

2.1 The Duffing Resonator 9

2.2 Baseband Equivalent Resonator Model 11

2.2.1 Second-Order Baseband Equivalent Resonator Model 11

2.2.2 First-Order Baseband Equivalent Resonator Model 13

2.2.3 Baseband Resonator Model with Noise 14

2.3 Non-Monte Carlo Method for Characterizing the Frequency Fluctuations 17

2.3.1 Resonance Frequency Variance in the Linear Regime 19

2.3.2 Bifurcation Frequency Variance in the Nonlinear Regime . . . 22

Chapter 3: Validation of the Method and Approximations **28**

3.1 Validating the First-Order Baseband Approximation 28

3.1.1 Verifying the Deterministic Baseband Model 28

3.1.2 Verifying the Stochastic Baseband Model 32

3.2 Verification of the non-Monte Carlo Method via Monte Carlo Simulations . . . 36
3.2.1 Verification for the Linear Regime . . . 37
3.2.2 Verification for the Nonlinear Regime . . . 43
3.3 Method Analysis . . . 52
3.3.1 Driving the System with Fixed Frequency Input . . . 52
3.3.2 Analyzing the Effect of Sweep Speed . . . 55

Chapter 4: Results **58**
4.1 Comparison with Experimental Results . . . 58
4.1.1 Variability of f_u versus f_d . . . 58
4.1.2 Variability of f_u and f_d versus Motion Amplitude . . . 59
4.1.3 Variability of f_u and f_d versus Temperature . . . 60
4.2 Variability in the Linear and Nonlinear Regimes . . . 61

Chapter 5: Summary and Conclusion **64**

Bibliography **67**

LIST OF FIGURES

1.1 Magnitude response of the resonator with increasing input amplitude in the (a) linear regime (b) nonlinear regime (c) nonlinear regime with hysteresis (not to scale). 6

2.1 Computationally obtained (a) Magnitude (normalized) and (b) phase response (with a $-\frac{\pi}{2}$ shift) in the linear and nonlinear regimes for forward and backward sweeps 20

2.2 Flowchart of the procedure of obtaining the resonance frequency variance for the resonator operating in the linear regime via the non-Monte Carlo method 21

2.3 Flowchart of the procedure of obtaining the bifurcation frequency variance for the upper branch of the resonator operating in the nonlinear regime via the non-Monte Carlo method 23

2.4 The staircase fractional frequency input (a) and the resulting output amplitude (b) for the backward frequency sweep. 24

2.5 Flowchart of the procedure of obtaining the bifurcation frequency variance for the lower branch of the resonator operating in the nonlinear regime via the non-Monte Carlo method 26

3.1 Theoretically obtained magnitude (a) and phase (c) responses of the first-order baseband and second-order passband models and their respective relative errors (b), (d) 29

3.2 Numerically obtained magnitude (a) and phase (c) responses of the linear first-order baseband and second-order passband models and their respective relative errors (b), (d) 30

3.3 Magnitude (a) and phase (c) responses of the first-order baseband and second-order passband nonlinear models with forward frequency sweep and their respective relative errors (b), (d) 31
3.4 Numerically obtained magnitude (a) and phase (c) responses of the first-order baseband and second-order passband nonlinear models with backward frequency sweep and their respective relative errors (b), (d) 32
3.5 Histograms for the resonance frequency obtained using data obtained via the baseband (a) and passband (b) stochastic models 33
3.6 Histograms for the f_d bifurcation frequency obtained using data obtained via the baseband (a) and passband (b) stochastic models . . . 34
3.7 Histograms for the f_u bifurcation frequency obtained using data obtained via the baseband (a) and passband (b) stochastic models . . . 35
3.8 Normalized standard deviations of the real (a) and imaginary (b) parts of $s_o^b(t)$ obtained via both the Monte Carlo and non-Monte Carlo methods and their relative errors (c), (d) 38
3.9 Normalized standard deviations of the amplitude (a) of $s_o^b(t)$ obtained via both the Monte Carlo and non-Monte Carlo methods and their relative error (b) 39
3.10 Normalized standard deviations of the phase (a) of $s_o^b(t)$ obtained via both the Monte Carlo and non-Monte Carlo methods and their relative error (b) 40
3.11 Normalized phase response (a) fractional resonance frequency (c) standard deviations for the Monte Carlo and non-Monte Carlo methods versus number of Monte Carlo realizations, and their errors (b), (d) 42
3.12 Normalized standard deviations of the real (a) and imaginary (b) parts of $s_o^b(t)$ for the forward sweep obtained via both the Monte Carlo and non-Monte Carlo methods and their relative errors (c), (d) 43

3.13 Normalized standard deviations of the real (a) and imaginary (b) parts of $s_o^b(t)$ for the backward sweep obtained via both the Monte Carlo and non-Monte Carlo methods and their relative errors (c), (d) 45
3.14 Ellipsoids showing the regions for the real and imaginary parts for fixed drive frequencies (fractional) of (a) $y = 2.5x10^{-3}$, (b) $y = 2.3x10^{-3}$, (c) $y = 1.5x10^{-3}$ and (d) $y = 1x10^{-3}$ 46
3.15 Ellipsoids obtained via the non-Monte Carlo method for various driving (fractional) frequencies 47
3.16 Amplitude variance for forward sweep obtained via both methods . . 48
3.17 Amplitude variance for backward sweep obtained via both methods . 49
3.18 Fractional bifurcation frequency standard deviation for the upper branch (y_u) (a) for the Monte Carlo and non-Monte Carlo methods versus number of Monte Carlo realizations, and their error (b) 50
3.19 (a) Fractional bifurcation frequency standard deviation for the lower branch (y_d) for various selected values A for A_d for the Monte Carlo and non-Monte Carlo methods versus number of Monte Carlo realizations, and (b) the standard deviations obtained for each selected value normalized by the non-Monte Carlo standard deviation for y_d . 51
3.20 Monte Carlo standard deviations of the real part of the output (a), imaginary part (b), amplitude (c) and phase (d) obtained via a frequency sweep, compared with results obtained via fixed frequency simulations of the system operating in the linear regime 53
3.21 Monte Carlo standard deviations of the real part of the output (a), imaginary part (b), amplitude (c) and phase (d) obtained via a forward frequency sweep, compared with results obtained via fixed frequency simulations of the system operating in the nonlinear regime . 54

3.22 Non-Monte Carlo standard deviations of the real part of the output (a), imaginary part (b), amplitude (c) and phase (d) obtained via a forward frequency sweep, compared with results obtained via fixed frequency simulations of the system operating in the nonlinear regime 55
3.23 Normalized standard deviations for f_o (a) and f_u (b) versus sweep speed obtained via both the Monte Carlo and Non-Monte Carlo techniques 56

4.1 $\sigma[y_o]$, $\sigma[y_u]$ and $\sigma[y_d]$ versus normalized drive amplitude (a) and $\sigma[y_o]$, $\sigma[y_u]$ and $\sigma[y_d]$ versus normalized motion amplitude (b) 59
4.2 Temperature dependence of $\sigma[y_u]$ and $\sigma[y_d]$ 60
4.3 $\sigma[y_u]$ and $\sigma[y_d]$ versus normalized drive amplitude (a) and $\sigma[y_u]$ and $\sigma[y_d]$ versus normalized motion amplitude (b) 62

ABBREVIATIONS

MC	Monte Carlo
PSD	Power Spectral Density
NEMS	Nanoelectromechanical Systems

Chapter 1

BACKGROUND

1.1 Introduction

Nanomechanical resonant sensors have shown tremendous potential for mass sensitivity in the past decade. Single protein molecule detection [Hanay et al., 2012] and yoctogram mass resolutions [Chaste et al., 2012] have been achieved through innovative techniques. In most applications of resonant sensors the resonators operate in the linear regime, where changes in mass and force are detected by tracking the shift in resonance frequency. Decreasing the device size can increase sensitivity and improve performance of the resonator. This, however, comes to the detriment of the linear operating range which diminishes with decreasing device size. The resonator in turn begins to exhibit nonlinear behavior even for the smallest drive levels needed for the sensors to operate properly [Maillet et al., 2018, Yuksel et al., 2019]. An alternative to this option is operating the resonator in the nonlinear regime, which displays the advantage of an increased dynamic range, as recently shown in a robust closed-loop setup [Yuksel et al., 2019]. In the nonlinear regime, the resonator displays a hysteretic response in a certain frequency region, the boundaries of which are called the bifurcation frequencies. Instead of the resonance frequency which is not directly accessible in the nonlinear regime, the shift in the bifurcation frequencies is tracked to detect the changes in mass or force [Maillet et al., 2018, Yuksel et al., 2019].

To evaluate the performance boundaries of the nonlinear resonator, a characterization of the fluctuations in the bifurcation frequencies due to various sources of noise is necessary. Understanding the sensitivity limits of the nonlinear resonator is of great importance in gauging their potential and comparing them to the resonators operating in the linear regime. Recent work has focused on experimentally characterizing the bifurcation frequency noise by employing open-loop frequency sweeps [Maillet et al., 2018]. Although it sheds light on various noise phenomena, this technique needs hundreds of sweeps to collect an adequate number of data for a statistically relevant characterization, making it time consuming and expensive. A new technique which can computationally perform the noise characterization of the bifurcation frequencies in a quicker manner while providing similar results would facilitate cheap and quick characterizations for various sensor scenarios. It would help decipher all the noise phenomena and performance restricting factors in nonlinear resonators, while saving the cost of expensive and time consuming experimental techniques.

One way to computationally characterize the bifurcation frequency fluctuations would be to use straightforward Monte Carlo (MC) simulations. This would be done by performing the computational equivalent of the experimental open-loop frequency sweeps in [Maillet et al., 2018], where random number generators are employed to emulate the noise sources in the dynamical system modeled by numerical differential equations. Similar to the experimental technique, a large number of computational frequency sweeps are necessary to generate an adequate number of data for proper mean and variance computation. The MC method indeed offers advantages compared to the experimental open-loop sweep method, but it also comes with a huge computational cost. One of its issues stems from the two time-scale behavior of the system, where the events of interest occur at a time scale much slower than the cycle time of the resonator, which is a bottleneck in the computation process and highly increases cost. Another issue arises due to the nature of the MC technique, where a large number of sweeps is required to get proper results.

In this thesis, we propose a computational technique which effectively tackles both of these issues. To tackle the first problem, we use the baseband equivalent representation for the Duffing resonator. The baseband equivalent (also known as envelope following) is a well-known complex amplitude representation. With this formulation, the system works with a much slower cycle time while accurately representing the noise phenomena of interest, thus drastically improving computation time and not compromising the results of the technique. Furthermore, to handle the second problem of the large number of necessary sweeps, we introduce a non-MC sweep formulation which can achieve computational characterization with only one frequency sweep as opposed to many. This unique method is based on a previously proposed noise analysis technique for analog circuits [Demir and Sangiovanni-Vincentelli, 1998]. This non-MC technique discards the random number generator altogether by directly computing the necessary information without the requirement of forming an ensemble. While a purely analytical evaluation of sensor performance is prohibited by the nonlinear nature of the resonator combined with stochastic noise, this proposed technique represents a semi-analytical method and is open to rigorous reasoning.

Previous work has concentrated on a theoretical analysis of the fluctuations in a Duffing resonator. In [Buks and Yurke, 2006], a frequency domain analysis method is presented, where instead of a frequency sweep, the system is analyzed only at a fixed frequency point. The fact that our method uses a dynamic sweep gives it the edge over its fixed operating point counterpart, due to its capability for noise characterizations under various dynamic sensing schemes, e.g., when drive frequency is time-varying and continually updated in a closed-loop setup [Maillet et al., 2018, Yuksel et al., 2019]. It also means that stochastic characterizations for a range of drive frequencies can be computed at once in a single sweep instead of only at a fixed frequency point, making our non-MC technique a more advantageous and powerful characterization method.

We note that Duffing resonators in a self-sustaining oscillator configuration have been previously considered and analyzed in the literature [Greywall et al., 1994, Yurke et al., 1995, Kenig et al., 2012, Demir and Hanay, 2018], and are beyond the scope of this work.

This thesis is organized as follows. In the rest of Chapter 1 we provide a brief background on oscillatory systems and their behavior in the linear and nonlinear oscillation regimes. In Chapter 2 we go into the theory behind the proposed technique. First, we introduce the Duffing resonator model, which is the model that best captures the behavior of nonlinear nanomechanical resonators [Lifshitz and Cross, 2008]. Then, we derive the baseband equivalent resonator model and finally, we introduce the non-Monte Carlo method for characterizing the frequency fluctuations in the Duffing resonator.

In Chapter 3, we verify if the approximations employed in the non-Monte Carlo technique correctly capture the properties of the system. We first validate the deterministic and stochastic baseband equivalent model. Then, we proceed to use Monte Carlo simulations to verify that the non-Monte Carlo technique is accurate. We analyze the effect of factors such as frequency sweep speed and number of realizations in the results obtained via both the Monte Carlo and non-Monte Carlo methods.

In Chapter 4, we use the proposed non-MC technique to examine the performance of the Duffing resonator in the nonlinear regime as opposed to the performance in the linear regime. Then, we proceed to compare our results with experimental results presented in literature. Finally, our conclusions and possible future work are discussed in Chapter 5.

1.2 Oscillatory Systems

The material in this section is a summary of the Small Oscillations chapter from [Landau and Lifshitz, 1976].

Oscillatory systems are mechanical systems that display oscillations around a position of stable equilibrium. One category of motion for these types of systems are forced oscillations in a system with friction and a periodic force input. These systems start to display nonlinear behavior with increasing input amplitude.

1.2.1 Linear Oscillations

When the driving input of an oscillating system has a small amplitude, lower approximations for its potential and kinetic energies, and thus, its equations of motion are enough to describe the system well. In this case, the equation describing the system driven with some certain amplitude C, frequency γ and under friction (damping) can be described as follows:

$$\frac{d^2 s_o(t)}{dt^2} + 2\lambda \frac{ds_o(t)}{dt} + \omega_o^2 s_o(t) = \frac{C}{m} cos(\gamma t) \tag{1.1}$$

where $s_o(t)$ is the deviation from equilibrium position, λ represents the damping coefficient (where $\lambda = \frac{\omega_o}{2Q}$), m is the mass and ω_o is the resonance frequency. The solution to Eqn. (1.1) is in the following form:

$$s_o(t) = ae^{-\lambda t}cos(\omega t + \alpha) + A_r cos(\gamma t + \delta) \tag{1.2}$$

where a, α, A_r and δ can all be determined by using the system parameters above. Note that the first term of $s_o(t)$ in Eqn. (1.2) decays with time, so the expression for the steady-state output $s_{oss}(t)$ will be:

$$s_{oss}(t) = A_r cos(\gamma t + \delta) \tag{1.3}$$

where

$$A_r = \frac{C}{m\sqrt{(\omega_o^2 - \gamma^2)^2 + 4\lambda^2\gamma^2}} \tag{1.4}$$

$$\delta = tan^{-1}\frac{2\lambda\gamma}{(\gamma^2 - \omega_o^2)} \tag{1.5}$$

The expression in Eqn. (1.4) describes the amplitude of the steady-state oscillations in the output $s_o(t)$ and their dependence on the system parameters and driving signal amplitude and frequency. As can be inferred, the oscillation amplitude A_r increases as γ approaches ω_o. The maximum is achieved when: $\gamma = \sqrt{\omega_o^2 - 2\lambda^2}$. For $\lambda \ll \omega_o$ this value is almost equal to ω_o.

If we consider the case where the system is being driven by a frequency near resonance $\gamma = \omega_o + \epsilon$ with ϵ being small and assuming that $\lambda << \omega_o$, the following approximation for the output amplitude A_r of the oscillations of the system driven around resonance frequency can be made:

$$A_r = \frac{C}{2m\omega_o\sqrt{\epsilon^2 + \lambda^2}} \tag{1.6}$$

1.2.2 Nonlinear Oscillations

When the system is driven with higher amplitudes, the expansion of the expression for the potential and kinetic energies of the system needs to include higher order

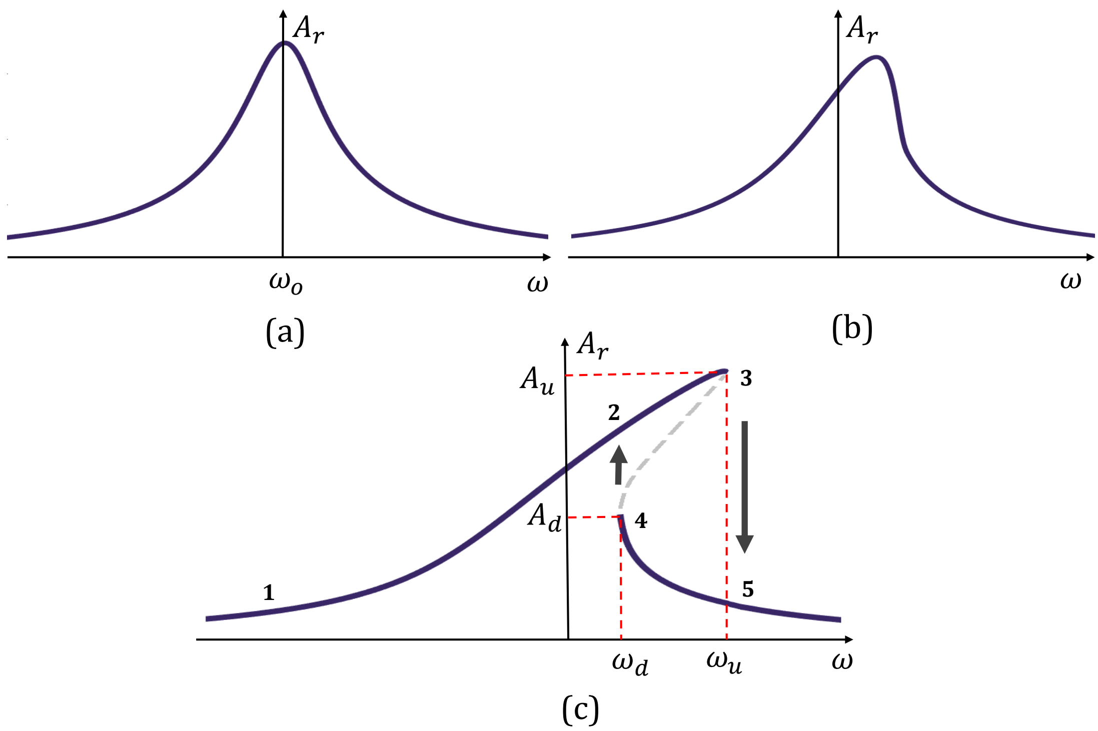

Figure 1.1: Magnitude response of the resonator with increasing input amplitude in the (a) linear regime (b) nonlinear regime (c) nonlinear regime with hysteresis (not to scale).

terms in order to describe the system appropriately. If we examine the expansion up to the third-order, we get the following expression:

$$\frac{d^2 s_o(t)}{dt^2} + 2\lambda \frac{ds_o(t)}{dt} + \omega_o^2 s_o(t) = \frac{C}{m} cos(\gamma t) - \beta s_o(t)^2 - \alpha s_o(t)^3 \tag{1.7}$$

where β and α are the coefficients for the second and third-order terms, respectively. In this case, the term for the new eigenfrequency ω_n is a shift from the original resonance frequency depending on amplitude, satisfying the following expression:

$$\omega_n = \omega_o + \kappa A_r^2 \tag{1.8}$$

where κ is a constant dependent on the two nonlinear coefficients α and β:

$$\kappa = \frac{3\alpha}{8\omega_o} - \frac{5\beta^2}{12\omega_o^3} \tag{1.9}$$

We want to quantify what happens when the driving frequency γ is in the vicinity of the resonance value, i.e. $\gamma = \omega_o + \epsilon$. That can be done without considering

Eqn. (1.7) above [Landau and Lifshitz, 1976]. If we look at the expression for the amplitude A_r in the solution to the linear approximation (Eqn. (1.6)), and replace ω_o with the new eigenfrequency $\omega_o + \kappa A_r^2$ in the ϵ term, we obtain a cubic equation for A_r^2:

$$A_r^2[(\epsilon - \kappa A_r^2)^2 + \lambda^2] = \frac{C^2}{4m^2\omega_o^2} \tag{1.10}$$

For small C, A_r also has a small amplitude, so if we ignore the powers of A_r that are greater than two, we obtain the same expression as that in Eqn. (1.6) for the linear case, and the amplitude frequency plot looks like the one in Figure 1.1.a. With increasing C, the curve is not symmetrical as in the linear case anymore. It shifts with an amount of ϵ to the left or right, depending on the sign of κ (Figure 1.1.b). After the amplitude A_r crosses a certain threshold A_s which we shall call the spinodal point [Maillet et al., 2018], a new phenomenon appears. The system begins to exhibit hysteresis. Eqn. (1.10) has three real roots in this region. Thus, there is an interval in which different values of oscillation amplitudes are possible (Figure 1.1.c). Given that the middle branch (from point 3 to 4) corresponds to unstable oscillations [Landau and Lifshitz, 1976], there are two different amplitudes of stable oscillation possible in that range of frequencies. In order to determine this range of frequencies, we need to find the frequency that corresponds to points 3 and 4 in Figure 1.1.c. For this, we find the points where $\frac{dA_r}{d\epsilon} = \infty$. That gives us the expressions for the two bifurcation frequencies, the one in the lower branch at point 4 (ω_d) and the one in the upper branch at point 3 (ω_u):

$$\omega_u = \omega_o + 2\kappa A_r^2 - \sqrt{(\kappa A_r^2)^2 - \lambda^2} \tag{1.11}$$

$$\omega_d = \omega_o + 2\kappa A_r^2 + \sqrt{(\kappa A_r^2)^2 - \lambda^2} \tag{1.12}$$

Eqns. (1.11) and (1.12) are very useful in the sense that they give us the relationship between the oscillation amplitude and the bifurcation frequencies.

To find the greatest amplitude, we look at the point where $\frac{dA_r}{d\epsilon} = 0$, which is:

$$A_{max} = \frac{C}{2m\omega_o\lambda} \tag{1.13}$$

Finally, we are interested in the drive and output amplitudes at the point where this behavior begins (onset of hysteresis), which we call C_s and A_s, respectively. In terms of the system parameters, these two quantities can be expressed as:

$$A_s = \frac{1}{3^{1/4}}\sqrt{\frac{2\lambda}{\kappa}} \tag{1.14}$$

And replacing A_s in Eqn. (1.10) we get:

$$C_s = \frac{1}{3^{3/4}}\sqrt{\frac{32\lambda^2 m^2 \omega_o^2}{\kappa}} \tag{1.15}$$

Thus, C_s above is the drive amplitude which drives the system to hysteresis.

Chapter 2

THEORY

2.1 *The Duffing Resonator*

In order to be able to characterize the frequency fluctuations in its output, a good deterministic model for the resonator is required. For small excitation forces, these resonators behave just as the linear oscillator shown in Eqn. (1.1). For larger excitations, nonlinear effects cannot be ignored, and the behavior of the resonator is best captured by the equation for the Duffing resonator [Lifshitz and Cross, 2008], which is Eqn. (1.7) with $\beta = 0$.

The equation describing a Duffing resonator is given below

$$\frac{d^2 s_o(t)}{dt^2} + \frac{\omega_o}{Q}\frac{ds_o(t)}{dt} + \omega_o^2 s_o(t) + \alpha s_o(t)^3 = \frac{1}{m} s_i(t) \tag{2.1}$$

where $s_o(t)$ is the displacement, $s_i(t)$ is the input force, ω_o is the resonance frequency, m is the resonator mass, Q is the quality factor and α is the coefficient of the cubic Duffing term.

As discussed in Section 1.2, for small excitations the resonator operates in the linear regime with magnitude response (versus drive frequency) as shown in Figure 1.1.a and linewidth

$$\Gamma = \frac{\omega_o}{Q} \tag{2.2}$$

For higher drive amplitudes, the resonator exhibits nonlinear behavior. The magnitude response is no longer symmetrical. Instead, it leans on one side as in Figure 1.1.b, depending on the sign of α [Landau and Lifshitz, 1976]. When the motion amplitude is above the spinodal point (A_s), the system exhibits hysteresis, where the amplitude of motion depends on which side the drive frequency is swept from. With a forward sweep of the input frequency (low to high frequency), the upper branch of the response in Figure 1.1.c is observed. The curve goes through points 1, 2 and 3 in the figure, only then to jump to point 5. With a backward sweep (high to low frequency), the 5-4-2-1 trajectory is observed. The bifurcation points at the jump frequencies from 3 to 5, ω_u, and from 4 to 2, ω_d, shown in Eqn. (1.12) are of interest. These bifurcation frequencies can be related to their respective motion amplitudes A_u and A_d as shown in Eqns. (1.12) and (1.11) where, in the case of the Duffing resonator, the parameter κ is:

$$\kappa = \frac{3\alpha}{8\omega_o} \tag{2.3}$$

The drive input to the resonator is of the form

$$s_i(t) = A_i \cos(\omega_o t + \int_0^t \Delta\omega_i(\tau)d\tau) = A_i \cos(\omega_o t + \theta_i(t)) \tag{2.4}$$

where A_i is the drive amplitude, $\Delta\omega_i(t)$ is the time-varying frequency shift and

$$\theta_i(t) = \int_0^t \Delta\omega_i(\tau)d\tau \tag{2.5}$$

is the phase deviation. $s_i(t)$ is expressed as the real part of a complex signal as follows

$$s_i(t) = \mathtt{Re}[A_i\, e^{j\theta_i(t)} e^{j\omega_o t}] \tag{2.6}$$

where $s_i^b(t) = A_i\, e^{j\theta_i(t)}$ is the complex envelope, a baseband signal centered around zero frequency, contrary to $s_i(t)$ [Benedetto and Biglieri, 1999]. $s_i(t)$ can be expressed in terms of its complex envelope

$$s_i(t) = \tfrac{1}{2}[e^{j\omega_o t} s_i^b(t) + e^{-j\omega_o t} s_i^b(t)^*] \tag{2.7}$$

where $\cdot^*$ denotes complex conjugate.

In this treatment, we assume that both the drive input and the resonator response are signals centered around ω_o (and $-\omega_o$). All other frequency components are filtered by the high-Q resonator. Thus, the resonator output can also be expressed as

$$s_o(t) = \tfrac{1}{2}[e^{j\omega_o t} s_o^b(t) + e^{-j\omega_o t} s_o^b(t)^*] \tag{2.8}$$

where $s_o^b(t) = Ae^{j\theta_r(t)}$ is its complex envelope, with A and θ_r being its amplitude and phase, respectively.

2.2 Baseband Equivalent Resonator Model

In the original Duffing Equation (Eqn. (2.1)), both the input and output are passband signals, i.e. they are centered around a higher nonzero frequency. For an easier treatment and increased computational efficiency, we will be deriving the baseband-equivalent representation of this system, and then further simplifying it to a first-order model. In this derivation, we follow the procedure presented in [Demir, 2021] for a linear resonator and generalize it to the case of a Duffing resonator.

2.2.1 Second-Order Baseband Equivalent Resonator Model

The passband signals for the input and output in Eqn. (2.1) can be expressed in terms of their baseband counterparts as shown in Eqns. (2.7) and (2.8). By replacing Eqns. (2.7) and (2.8) in Eqn. (2.1), we obtain:

$$\frac{1}{2}e^{j\omega_o t}dS(t) + \frac{1}{2}e^{-j\omega_o t}dS(t)^* + \alpha\, s_o(t)^3 = \frac{1}{2m}[e^{j\omega_o t}s_i^b(t) + e^{-j\omega_o t}s_i^b(t)^*] \tag{2.9}$$

where

$$dS(t) = \frac{d^2 s_o^b(t)}{dt^2} + (j2\omega_o + \frac{\omega_o}{Q})\frac{ds_o^b(t)}{dt} + j\frac{\omega_o^2}{Q}s_o^b(t) \tag{2.10}$$

and

$$\begin{aligned}\alpha\, s_o(t)^3 = \tfrac{1}{8}\alpha\, \big[&e^{j3\omega_o t}s_o^b(t)^3 + 3e^{j\omega_o t}s_o^b(t)|s_o^b(t)|^2 \\ &+3e^{-j\omega_o t}|s_o^b(t)|^2\, s_o^b(t)^* + e^{-j3\omega_o t}(s_o^b(t)^*)^3\big]\end{aligned} \tag{2.11}$$

If we look at Eqn. (2.9), we can observe that it is only composed of terms around ω_o and -ω_o frequencies or their higher harmonics. Let us now integrate Eqn. (2.9) with $e^{-j\omega_o t}$ in one period $\frac{2\pi}{\omega_o}$ as follows:

$$\begin{aligned}&\int_0^{\frac{2\pi}{\omega_o}} e^{-j\omega_o t}(\frac{1}{2}e^{j\omega_o t}dS(t) + \frac{1}{2}e^{-j\omega_o t}dS(t)^* + \alpha\, s_o(t)^3)dt \\ &\qquad = \frac{1}{2m}(\int_0^{\frac{2\pi}{\omega_o}} e^{-j\omega_o t}(e^{j\omega_o t}s_{in}^b(t) + e^{-j\omega_o t}s_{in}^b(t)^*)dt)\end{aligned} \tag{2.12}$$

First, we assume that the complex envelopes $s_o^b(t)$ and $s_i^b(t)$ vary much slower in time than their passband counterparts. For that reason, we assume them to be constant in one period of $e^{-j\omega_o t}$. As such, the terms inside $dS(t)$ and $dS(t)^*$, as well as $s_i^b(t)$

are taken as constants and they are taken outside the integral. Thus, we are left with the following expression

$$\frac{1}{2}dS(t)\int_0^{\frac{2\pi}{\omega_o}} e^{-j\omega_o t}e^{j\omega_o t}dt + \frac{1}{2}dS(t)^*\int_0^{\frac{2\pi}{\omega_o}} e^{-j\omega_o t}e^{-j\omega_o t}dt + \int_0^{\frac{2\pi}{\omega_o}} \alpha s_o(t)^3 e^{-j\omega_o t}dt$$
$$= \frac{1}{2m}s_{in}^b(t)\int_0^{\frac{2\pi}{\omega_o}} e^{-j\omega_o t}e^{j\omega_o t}dt + \frac{1}{2m}s_{in}^b(t)^*\int_0^{\frac{2\pi}{\omega_o}} e^{-j\omega_o t}e^{-j\omega_o t}dt \tag{2.13}$$

where

$$\int_0^{\frac{2\pi}{\omega_o}} \alpha s_o(t)^3 e^{-j\omega_o t}dt = \frac{\alpha}{8}\Bigg[s_o^b(t)^3\int_0^{\frac{2\pi}{\omega_o}} e^{-j\omega_o t}e^{j3\omega_o t}dt + s_o^b(t)|s_o^b(t)|^2\int_0^{\frac{2\pi}{\omega_o}} 3e^{-j\omega_o t}e^{j\omega_o t}dt$$
$$+|s_o^b(t)|^2\, s_o^b(t)^*\int_0^{\frac{2\pi}{\omega_o}} 3e^{-j\omega_o t}e^{-j\omega_o t}dt + (s_o^b(t)^*)^3\int_0^{\frac{2\pi}{\omega_o}} e^{-j\omega_o t}e^{-j3\omega_o t}dt\Bigg] \tag{2.14}$$

The inner product in one period $\frac{2\pi}{\omega_o}$ of two complex exponentials with frequencies $k\omega_o$ and $l\omega_o$ is

$$\int_0^{\frac{2\pi}{\omega_o}} e^{jk\omega_o t}e^{-jl\omega_o t}dt = \begin{cases} \int_0^{\frac{2\pi}{\omega_o}} 1dt & \text{if} \quad k = l \\ 0 & \text{if} \quad k \neq l \end{cases} \tag{2.15}$$

Thus, due to the orthogonality of complex exponentials of the harmonics of a frequency, only the baseband part of the terms around the ω_o frequency will remain, while the others will vanish

$$\frac{dS(t)}{2}\int_0^{\frac{2\pi}{\omega_o}} e^{-j\omega_o t}e^{j\omega_o t}dt + \frac{3\alpha}{8}s_o^b(t)|s_o^b(t)|^2\int_0^{\frac{2\pi}{\omega_o}} e^{-j\omega_o t}e^{j\omega_o t}dt = \frac{1}{2m}s_{in}^b(t)\int_0^{\frac{2\pi}{\omega_o}} e^{-j\omega_o t}e^{j\omega_o t}dt \tag{2.16}$$

Removing the integral parts from both sides, we obtain:

$$\frac{dS(t)}{2} + \frac{3\alpha}{8}s_o^b(t)|s_o^b(t)|^2 = \frac{1}{2m}s_{in}^b(t) \tag{2.17}$$

or

$$\frac{d^2 s_o^b(t)}{dt^2} + (j2\omega_o + \frac{\omega_o}{Q})\frac{ds_o^b(t)}{dt} + j\frac{\omega_o^2}{Q}s_o^b(t) + \frac{3\alpha}{4}s_o^b(t)|s_o^b(t)|^2 = \frac{1}{m}s_{in}^b(t) \tag{2.18}$$

Eqn. (2.18) is the second-order baseband differential equation describing the Duffing resonator.

2.2.2 First-Order Baseband Equivalent Resonator Model

In the baseband system, the frequency of operation ω is very low compared to ω_o. Using this fact ($\omega \ll \omega_o$), we can convert Eqn. (2.18) into an approximated first-order baseband model.

The approximation $\omega \ll \omega_o$ gives us two results:

1. In the second term in Eqn. (2.18):

$$(j2\omega_o + \frac{\omega_o}{Q})\frac{ds_o^b(t)}{dt}$$

we note that the line-width $\frac{\omega_o}{Q}$ is much smaller than the $j2\omega_o$ term. Thus we can make the following approximation:

$$j2\omega_o + \frac{\omega_o}{Q} \approx j2\omega_o \tag{2.19}$$

2. We know that our baseband signal has the form

$$s_o^b(t) = Ae^{j\omega t}$$

Therefore, its first and second derivatives have the following form:

$$\frac{ds_o^b(t)}{dt} = j\omega Ae^{j\omega t} \tag{2.20}$$

and

$$\frac{d^2 s_o^b(t)}{dt^2} = -\omega^2 Ae^{j\omega t} \tag{2.21}$$

Since we know that $s_o^b(t)$ has bandwidth $\frac{\omega_o}{Q}$, we know that $|\omega|$ is limited by:

$$|\omega| \leq \frac{\omega_o}{Q} \tag{2.22}$$

Thus, the highest factor that the first derivative can multiply the function with is $\frac{\omega_o}{Q}$ and the factor induced by the second derivative is $(\frac{\omega_o}{Q})^2$. Using:

$$(\frac{\omega_o}{Q})^2 \ll \frac{\omega_o^2}{Q} \tag{2.23}$$

we can establish that the second derivative term also is small in comparison to the other terms, and remove it from the equation.

Thus, using these approximations we obtain the first-order baseband model for the Duffing resonator:

$$j2\omega_o \frac{ds_o^b(t)}{dt} + j\frac{\omega_o^2}{Q}s_o^b(t) + \frac{3\alpha}{4}s_o^b(t)|s_o^b(t)|^2 = \frac{1}{m}s_{in}^b(t) \tag{2.24}$$

or, by rearranging the terms

$$\frac{ds_o^b(t)}{dt} + \frac{\omega_o}{2Q}s_o^b(t) + \frac{3\alpha}{j8\omega_o}|s_o^b(t)|^2 s_o^b(t) = \frac{1}{j2m\omega_o}s_i^b(t) \tag{2.25}$$

Eqn. (2.25) is the first-order baseband differential equation describing the Duffing resonator.

2.2.3 Baseband Resonator Model with Noise

In this thesis, the effect of thermo-mechanical noise in the resonator output will be analyzed. This noise can be modeled as a white noise source with the following spectral density [Ekinci et al., 2004]:

$$S_{thm}(\omega) = \frac{2m\omega_o k_B T}{Q} \tag{2.26}$$

where k_B is Boltzmann's constant and T is the temperature in Kelvin.
In time domain, we will denote the noise signal as $n_{thm}(t)$. The noise will be added to the equation for the Duffing resonator as an additive term. Since we are working with the baseband equation, we will need to find the baseband equivalent to the input noise. Similar to the representations for our deterministic signals, we can express our passband noise signal as follows:

$$n_{thm}(t) = \frac{1}{2}(e^{j\omega_0 t}n_{thm}^b(t) + e^{-j\omega_0 t}n_{thm}^b(t)^*) \tag{2.27}$$

where n_{thm}^b is the baseband equivalent (complex envelope) of the passband noise signal. Thus, if we insert that expression as we did before in the original equation, we will obtain the equation for the baseband resonator model with noise as follows:

$$\frac{d}{dt}s_o^b(t) + \frac{\omega_0}{2Q}s_o^b(t) + \frac{3\alpha}{j8\omega_0}|s_o^b(t)|^2 s_o^b(t) = \frac{1}{j2m\omega_0}(s_i^b(t) + n_{thm}^b(t)) \tag{2.28}$$

where the noise is added as a scaled additive term in the right-hand side of the equation.

Deriving the Baseband Equivalent of Passband Noise

The material in this section is excerpted from [Benedetto and Biglieri, 1999].

The passband system has input noise with a power spectral density as in Eqn. (2.26). Since the input to the system is passband, we can consider the additive noise $S_{thm}(\omega)$ to be a passband white process. This is the power spectral density (PSD) of the signal $n_{thm}(t)$. The complex process $\mathring{n}_{thm}(t)$ in the following form is called the analytical signal related to $n_{thm}(t)$:

$$\mathring{n}_{thm}(t) = n_{thm}(t) + j\hat{n}_{thm}(t) \tag{2.29}$$

where $\hat{n}_{thm}(t)$ is the Hilbert transform of $n_{thm}(t)$ [Benedetto and Biglieri, 1999]. The analytical signal can also be represented as:

$$\mathring{n}_{thm}(t) = n^b_{thm}(t)e^{j\omega_o t} \tag{2.30}$$

where $n^b_{thm}(t)$ is the complex envelope, or the baseband equivalent of $n_{thm}(t)$. Our aim is to find the power spectral density of $n^b_{thm}(t)$, since we are working with the baseband-equivalent model. We will demonstrate it in a series of steps.

As mentioned above, since the noise $S_{thm}(\omega)$ is additive and the system itself is passband, the noise can be considered as a passband white noise signal. Then, observing that $\mathring{n}_{thm}(t)$ is the output of a LTI system with input $n_{thm}(t)$ and transfer function $2u(\omega)$, where $u(\omega)$ is the unit step function, we can easily find the power spectral density (PSD) for $\mathring{n}_{thm}(t)$. For a LTI system, given the input PSD $S_{in}(\omega)$ and the system transfer function $H(\omega)$, the output PSD $S_{out}(\omega)$ can be calculated as:

$$S_{out}(\omega) = S_{in}(\omega)|H(\omega)|^2 \tag{2.31}$$

Thus, the PSD of $\mathring{n}_{thm}(t)$ calculated this way gives us:

$$S_{\mathring{n}_{thm}}(\omega) = S_{thm}(\omega)|2u(\omega)|^2 = 4S_{thm}(\omega)u(\omega) \tag{2.32}$$

Thus, its PSD is four times the PSD of the input noise, but in this case it is one-sided. Then, we proceed to obtain the PSD for the complex envelope $n^b_{thm}(t)$. We can write it as (reformulating Eqn. (2.30)):

$$n^b_{thm}(t) = \mathring{n}_{thm}(t)e^{-j\omega_o t} \tag{2.33}$$

Its autocorrelation function is:

$$R_{n^b_{thm}} = E[\mathring{n}_{thm}(t+\tau)\mathring{n}^*_{thm}(t)]e^{-j\omega_o\tau} \tag{2.34}$$

$$R_{n^b_{thm}} = R_{\mathring{n}_{thm}} e^{-j\omega_o\tau} \tag{2.35}$$

Thus, given that the power spectral density of a signal is the Fourier Transform of its autocorrelation function, we have the autocorrelation of $n^b_{thm}(t)$ in terms of the autocorrelation of $\mathring{n}_{thm}(t)$ given as:

$$S_{n^b_{thm}}(\omega) = S_{\mathring{n}_{thm}}(\omega - \omega_o) \tag{2.36}$$

Since in this work we are working with a complex baseband signal $n^b_{thm}(t)$, we need to find the spectrum for both real and imaginary parts. Let's call the real part $n_{\mathrm{RE}}(t)$ and the imaginary part $n_{\mathrm{IM}}(t)$. It is known that [Benedetto and Biglieri, 1999]:

$$R_{n_{\mathrm{RE}}}(\tau) = R_{n_{\mathrm{IM}}}(\tau) \tag{2.37}$$

and

$$E[n_{\mathrm{RE}}(t+\tau)n_{\mathrm{IM}}(t)] = -E[n_{\mathrm{IM}}(t+\tau)n_{\mathrm{RE}}(t)] \tag{2.38}$$

Thus, we can obtain:

$$R_{n^b_{thm}}(\tau) = 2[R_{n_{\mathrm{RE}}}(\tau) + jR_{n_{\mathrm{IM}}n_{\mathrm{RE}}}(\tau)] \tag{2.39}$$

Since $R_{n^b_{thm}}(0)$ is a real quantity, it follows that:

$$E[n_{\mathrm{IM}}(t)n_{\mathrm{RE}}(t)] = 0 \tag{2.40}$$

which means that the real and imaginary parts of the noise process are uncorrelated. In addition, using Eqns. (2.38) and (2.40) we can conclude that:

$$E[|\tilde{n}(t)|^2] = 2E[|n_{\mathrm{RE}}(t)|^2] = 2E[|n_{\mathrm{IM}}(t)|^2] \tag{2.41}$$

Thus, the average power of the real and imaginary parts is equal to the power of the initial passband process $n_{thm}(t)$. In conclusion, the imaginary and real baseband noise components are uncorrelated bandlimited white noise signals with spectrum:

$$S_{\mathrm{RE}}(\omega) = S_{\mathrm{IM}}(\omega) = 2S_{thm}(\omega) \tag{2.42}$$

2.3 Non-Monte Carlo Method for Characterizing the Frequency Fluctuations

To characterize the resonance (for the linear regime) and bifurcation (for the nonlinear regime) frequency noise, we employ the time-domain non-Monte Carlo method proposed in [Demir and Sangiovanni-Vincentelli, 1998]. Since the output $s_o^b(t)$ is a complex valued signal, we define $s_{\mathrm{RE}}^o(t)$ and $s_{\mathrm{IM}}^o(t)$ to be its real and imaginary parts, respectively. The first-order baseband resonator with noise can be represented as a system of two coupled, real valued, nonlinear stochastic differential equations (NLSDEs) in $s_{\mathrm{RE}}^o(t)$ and $s_{\mathrm{IM}}^o(t)$. The baseband thermo-mechanical noise input appears as an additive term. The noise source is modeled in terms of the standard white Gaussian process, *i.e.,* the formal derivative of the Wiener process. The two coupled differential equations for the real and imaginary parts are as follows:

$$\frac{d}{dt}s_{\mathrm{RE}}^o(t) + \frac{\omega_0}{2Q}s_{\mathrm{RE}}^o(t) + \frac{3\alpha}{8\omega_0}|s_o(t)|^2 s_{\mathrm{IM}}^o(t) = \frac{1}{2m\omega_0}(s_{\mathrm{IM}}^i(t) + n_{\mathrm{IM}}(t)) \tag{2.43}$$

$$\frac{d}{dt}s_{\mathrm{IM}}^o(t) + \frac{\omega_0}{2Q}s_{\mathrm{IM}}^o(t) - \frac{3\alpha}{8\omega_0}|s_o(t)|^2 s_{\mathrm{RE}}^o(t) = -\frac{1}{2m\omega_0}(s_{\mathrm{RE}}^i(t) + n_{\mathrm{RE}}(t)) \tag{2.44}$$

where $s_{\mathrm{RE}}^i(t)$ and $s_{\mathrm{IM}}^i(t)$ are the real and imaginary parts of the input, respectively. The system in Eqns. (2.43) and (2.44) (described using $s_{\mathrm{RE}}^o(t)$ and $s_{\mathrm{IM}}^o(t)$) with additive noise can be compactly described as follows:

$$\mathbf{I}(\mathbf{s}^o(t), t) + \frac{d}{dt}\mathbf{Q}(\mathbf{s}^o(t)) + \mathbf{B}(\mathbf{s}^o(t), t)\xi(t) = 0 \tag{2.45}$$

where

$$\mathbf{I}(\mathbf{s}^o(t), t) = \begin{bmatrix} \frac{\omega_o}{2Q}s_{\mathrm{RE}}^o(t) + \frac{3\alpha}{8\omega_o}|s_o^b(t)|^2 s_{\mathrm{IM}}^o(t) - \frac{1}{2m\omega_o}s_{\mathrm{IM}}^i(t) \\ \frac{\omega_o}{2Q}s_{\mathrm{IM}}^o(t) - \frac{3\alpha}{8\omega_o}|s_o^b(t)|^2 s_{\mathrm{RE}}^o(t) + \frac{1}{2m\omega_o}s_{\mathrm{RE}}^i(t) \end{bmatrix}$$

$$\mathbf{Q}(\mathbf{s}^o(t)) = \begin{bmatrix} s_{\mathrm{RE}}^o(t) \\ s_{\mathrm{IM}}^o(t) \end{bmatrix}$$

$$\mathbf{B}(\mathbf{s}^o(t)) = \frac{1}{2m\omega_o}\sqrt{S_{\mathrm{RE}}(\omega)}\,\mathbf{I_2}$$

where $\mathbf{I_2}$ is the 2×2 identity matrix, $\xi(t)$ represents a vector of white Gaussian noise processes, and $\mathbf{s}^o(t)$ is the vector $[s_{\mathrm{RE}}^o(t)\ \ s_{\mathrm{IM}}^o(t)]^T$.

Using the small noise expansion [Demir and Sangiovanni-Vincentelli, 1998], the solution $\mathbf{s}^o(t)$ can be written as:

$$\mathbf{s}^o(t) = \mathbf{s}^o_s(t) + \mathbf{s}^o_n(t) \tag{2.46}$$

where $\mathbf{s}^o_s(t)$ represents the solution to the deterministic system in Eqn. (2.45) without noise and $\mathbf{s}^o_n(t)$ represents the perturbations due to noise. $\mathbf{s}^o_n(t)$ can be approximated as a Gaussian process with zero mean, *i.e.*, $\mathcal{E}[\mathbf{s}^o_n(t)] = 0$, where $\mathcal{E}[\cdot]$ is the expectation operator. It is assumed that the perturbation component $\mathbf{s}^o_n(t)$ is small compared to the deterministic solution $\mathbf{s}^o_s(t)$, an approximation routinely employed in noise characterization techniques. The covariance matrix $\mathbf{K}(t)$ of $\mathbf{s}^o_n(t)$, defined by $\mathbf{K}(t) = \mathcal{E}[\mathbf{s}^o_n(t)\, \mathbf{s}^o_n(t)^T]$, is shown in [Demir and Sangiovanni-Vincentelli, 1998] to be the solution of the following system of differential equations:

$$\frac{d}{dt}\mathbf{K}(t) = \mathbf{E}(t)\mathbf{K}(t) + \mathbf{K}(t)\mathbf{E}(t)^T + \mathbf{F}(t)\mathbf{F}(t)^T \tag{2.47}$$

$$\begin{aligned}
\mathbf{E}(t) &= -\mathbf{C}(t)^{-1}\mathbf{G}(t)\\
\mathbf{F}(t) &= -\mathbf{C}(t)^{-1}\mathbf{B}(t)\\
\mathbf{G}(t) = \left.\frac{\partial \mathbf{I}(\mathbf{s}^o(t), t)}{\partial \mathbf{s}^o(t)}\right|_{\mathbf{s}^o_s(t)}, &\quad \mathbf{C}(t) = \left.\frac{d\mathbf{Q}(\mathbf{s}^o(t))}{d\mathbf{s}^o(t)}\right|_{\mathbf{s}^o_s(t)}\\
\mathbf{B}(t) &= \mathbf{B}(\mathbf{s}^o_s(t), t)
\end{aligned} \tag{2.48}$$

where $\mathbf{G}(t)$ and $\mathbf{C}(t)$ are Jacobian matrices. The matrices for our first-order baseband nonlinear resonator model are as follows:

$$\begin{aligned}
\mathbf{G}(t) &= \begin{bmatrix} \frac{\omega_o}{2Q} + \frac{3\alpha}{4\omega_o} s^o_{\mathrm{RE}}(t) s^o_{\mathrm{IM}}(t) & \frac{3\alpha}{8\omega_o}(s^o_{\mathrm{RE}}(t)^2 + 3s^o_{\mathrm{IM}}(t)^2) \\ -\frac{3\alpha}{8\omega_o}(3s^o_{\mathrm{RE}}(t)^2 + s^o_{\mathrm{IM}}(t)^2) & \frac{\omega_o}{2Q} - \frac{3\alpha}{4\omega_o} s^o_{\mathrm{RE}}(t) s^o_{\mathrm{IM}}(t) \end{bmatrix}\\
\mathbf{C}(t) &= \mathbf{I_2}
\end{aligned} \tag{2.49}$$

These equations show that in order to obtain the covariance matrix of $\mathbf{s}^o_n(t)$, the deterministic solution $\mathbf{s}^o_s(t)$ to Eqn. (2.45), without noise must be computed first. This is done by using the fourth-order Runge-Kutta method for numerical integration [Süli and Mayers, 2003]. The solution to Eqn. (2.47) for the covariance matrix of $\mathbf{s}^o_n(t)$ is computed concurrently using the same numerical method. Finally, the time-varying covariance matrix is used to characterize the frequency fluctuations of the resonator. We compute the variance of our desired quantities: the resonance frequency in the linear operating regime of the resonator, and the bifurcation frequencies in the nonlinear regime. The procedure of obtaining these variances in the two regimes varies significantly, so both procedures are explained separately and in detail in the next two subsections.

2.3.1 Resonance Frequency Variance in the Linear Regime

The relationship between the phase and frequency in the linear resonator characteristics is key to obtaining the resonance frequency variance for the resonator operating in the linear regime. First, we derive the relationship between these two quantities and their variances, and then we describe the procedure with which they are obtained via the non-Monte Carlo method.

The phase of the resonator response is given by:

$$\theta_r(t) = \arctan \frac{s^o_{\mathrm{IM}}(t)}{s^o_{\mathrm{RE}}(t)} \tag{2.50}$$

Linearizing the above expression by using the Taylor series expansion around a time point t_0, we obtain:

$$\begin{aligned} \theta_r(t) &= a(t_0)s^o_{\mathrm{RE}}(t) + b(t_0)s^o_{\mathrm{IM}}(t) + c(t_0) \\ a(t_0) &= -\frac{s_{\mathrm{IM}}(t_0)}{s^2_{\mathrm{RE}}(t_0) + s^2_{\mathrm{IM}}(t_0)} \\ b(t_0) &= \frac{s_{\mathrm{RE}}(t_0)}{s^2_{\mathrm{RE}}(t_0) + s^2_{\mathrm{IM}}(t_0)} \end{aligned} \tag{2.51}$$

where $a(t_0)$ and $b(t_0)$ are the constant weights for the real and imaginary parts, respectively, and $c(t_0)$ contains all of the deterministic terms which are irrelevant in a variance computation and thus shall not be employed in this computation. We define $\mathbf{P}(t) = [a(t)\ \ b(t)]^T$, and then obtain the phase variance at t_0 as a function of the covariance matrix $\mathbf{K}(t_0)$ as follows:

$$\mathtt{var}[\theta_r(t_0)] = \mathbf{P}(t_0)^T\mathbf{K}(t_0)\mathbf{P}(t_0) \tag{2.52}$$

where, in our case, t_0 is chosen to be the time point at which the drive frequency is equal to the resonance frequency.

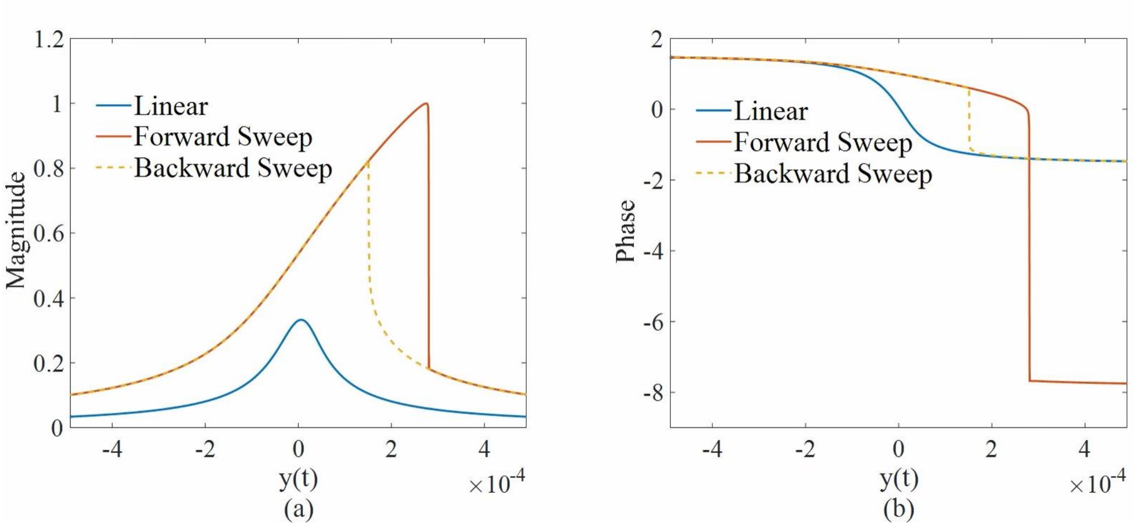

Figure 2.1: Computationally obtained (a) Magnitude (normalized) and (b) phase response (with a $-\frac{\pi}{2}$ shift) in the linear and nonlinear regimes for forward and backward sweeps

We next find the relationship between the phase and frequency. The baseband equation for the resonator operating in the linear regime (excluding the nonlinear term), is given by the following equation:

$$\frac{d}{dt}s_o^b(t) + \frac{\omega_o}{2Q}s_o^b(t) = \frac{1}{j2m\omega_o}s_i^b(t) \tag{2.53}$$

corresponding to the following transfer function in the frequency domain [Demir and Hanay, 2020]:

$$H(\omega) = \frac{Q}{m\,\omega_o^2}e^{-j\frac{\pi}{2}}\frac{1}{1+j\omega\frac{2Q}{\omega_o}} \tag{2.54}$$

Ignoring the constant $-\frac{\pi}{2}$ phase shift, the phase-frequency relationship follows:

$$\theta_r(\omega) = \arctan(-\tfrac{2Q}{\omega_o}\omega) \tag{2.55}$$

Around $\omega = 0$ (resonance frequency for the baseband resonator), the phase is almost a linear function of ω. Linearization around that point yields [Demir, 2021]:

$$\theta_r(\omega) \approx -\frac{2Q}{\omega_o}\omega \tag{2.56}$$

Finally, we use Eqns. (2.56) and (2.52) to obtain the relationship between the variance of phase and frequency at resonance, where $f_o = \frac{\omega_o}{2\pi}$:

$$\texttt{var}[f_o] = (\tfrac{f_o}{2Q})^2\texttt{var}[\theta_r(t_0)] = (\tfrac{f_o}{2Q})^2\mathbf{P}(t_0)^T\mathbf{K}(t_0)\mathbf{P}(t_0) \tag{2.57}$$

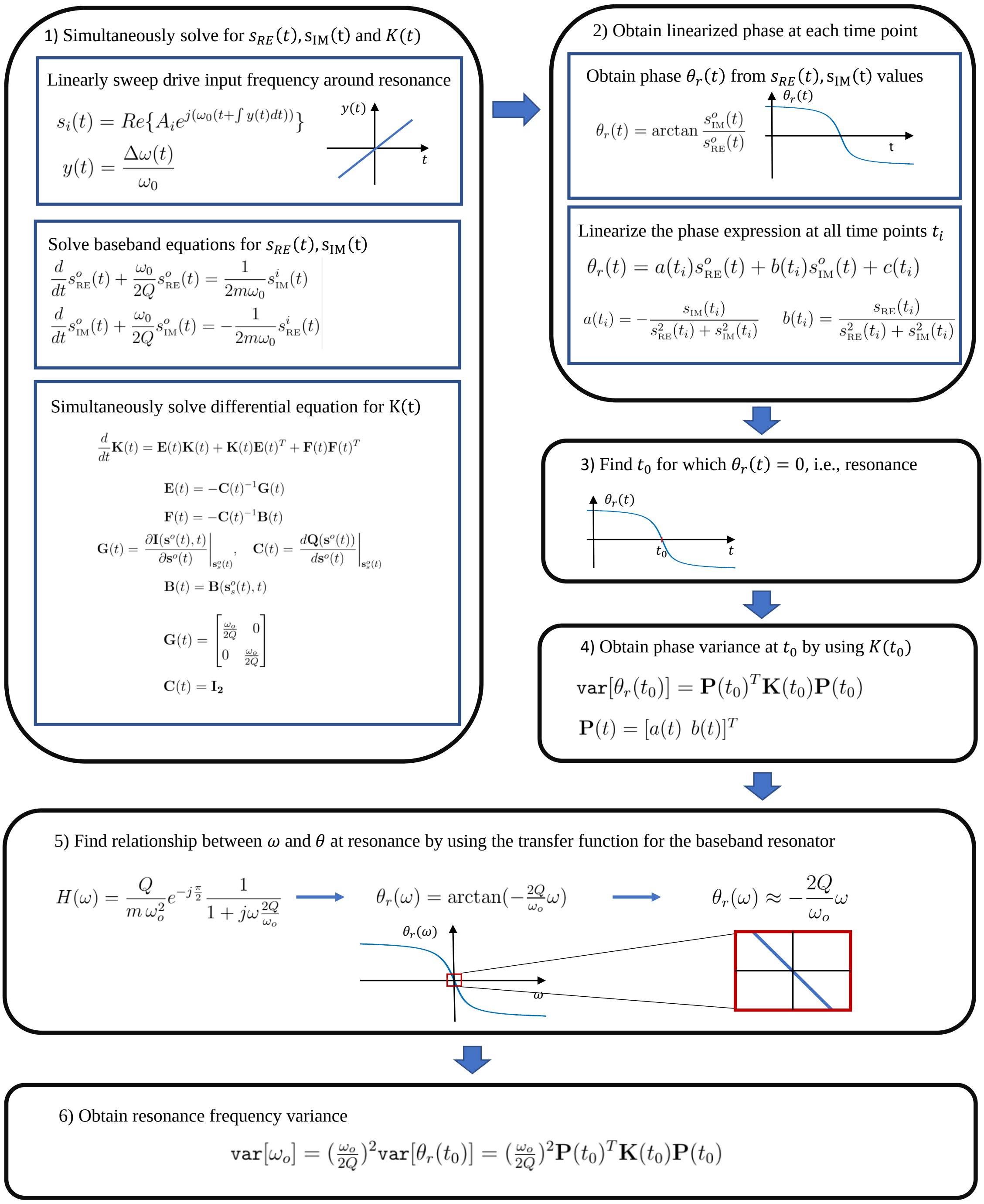

Figure 2.2: Flowchart of the procedure of obtaining the resonance frequency variance for the resonator operating in the linear regime via the non-Monte Carlo method

Next, we describe the exact procedure of obtaining the resonance frequency via the non-Monte Carlo method which is illustrated in detail in the flowchart in Figure 2.2. We first drive the system with a noiseless input with constant amplitude and a linear frequency sweep around the resonance frequency. This sweep results in the magnitude and phase responses shown in Figure 2.1 (curves for the linear case). Note that we add a $-\frac{\pi}{2}$ shift to the phase response. We then numerically determine the time point t_0 at which the phase crosses zero, which corresponds to drive frequency being equal to the resonance frequency, *i.e.,* we determine the time point corresponding to resonance frequency input. Then, we record the covariance matrix $\mathbf{K}(t_0)$ corresponding to the covariance of $\mathbf{s}_n^o(t)$ at resonance frequency. We recall that $\mathbf{K}(t)$ is computed concurrently with the noiseless sweep in a time synchronous manner. We next use $\mathbf{K}(t_0)$ to compute the phase variance, and finally convert it to resonance frequency variance using their relationship in Eqn. (2.57).

2.3.2 Bifurcation Frequency Variance in the Nonlinear Regime

In the nonlinear regime, the relationships between the bifurcation frequencies and their corresponding motion amplitudes, for ω_u and ω_d in Eqns. (1.12), are utilized to obtain the variances of the bifurcation frequencies $f_u = \frac{\omega_u}{2\pi}$ and $f_d = \frac{\omega_d}{2\pi}$.

The procedure for obtaining the variance of the upper branch bifurcation frequency f_u is as follows. First, we perform a linear low-to-high (forward) noiseless sweep of the drive frequency, resulting in the magnitude and phase responses shown in Figure 2.1 (curve for the forward sweep). We first aim to obtain A_u, the motion amplitude at f_u. Theoretically, that corresponds to the point where the amplitude drops with infinite slope. Determining this point proves to be very challenging, since using numerical gradient information in that region is not very robust. The obtained value depends on sweep speed and as such, it cannot give reliable results. An alternative point which accurately approximates A_u and at the same time can be consistently determined is needed. The new alternative amplitude is chosen to be the point at which the magnitude is maximum. As can be seen in Figure 2.1, the drop in amplitude for the forward sweep curve occurs immediately after the amplitude response reaches its maximum point. That shows it is in fact very close to A_u and it provides the benefit of reliable computation.

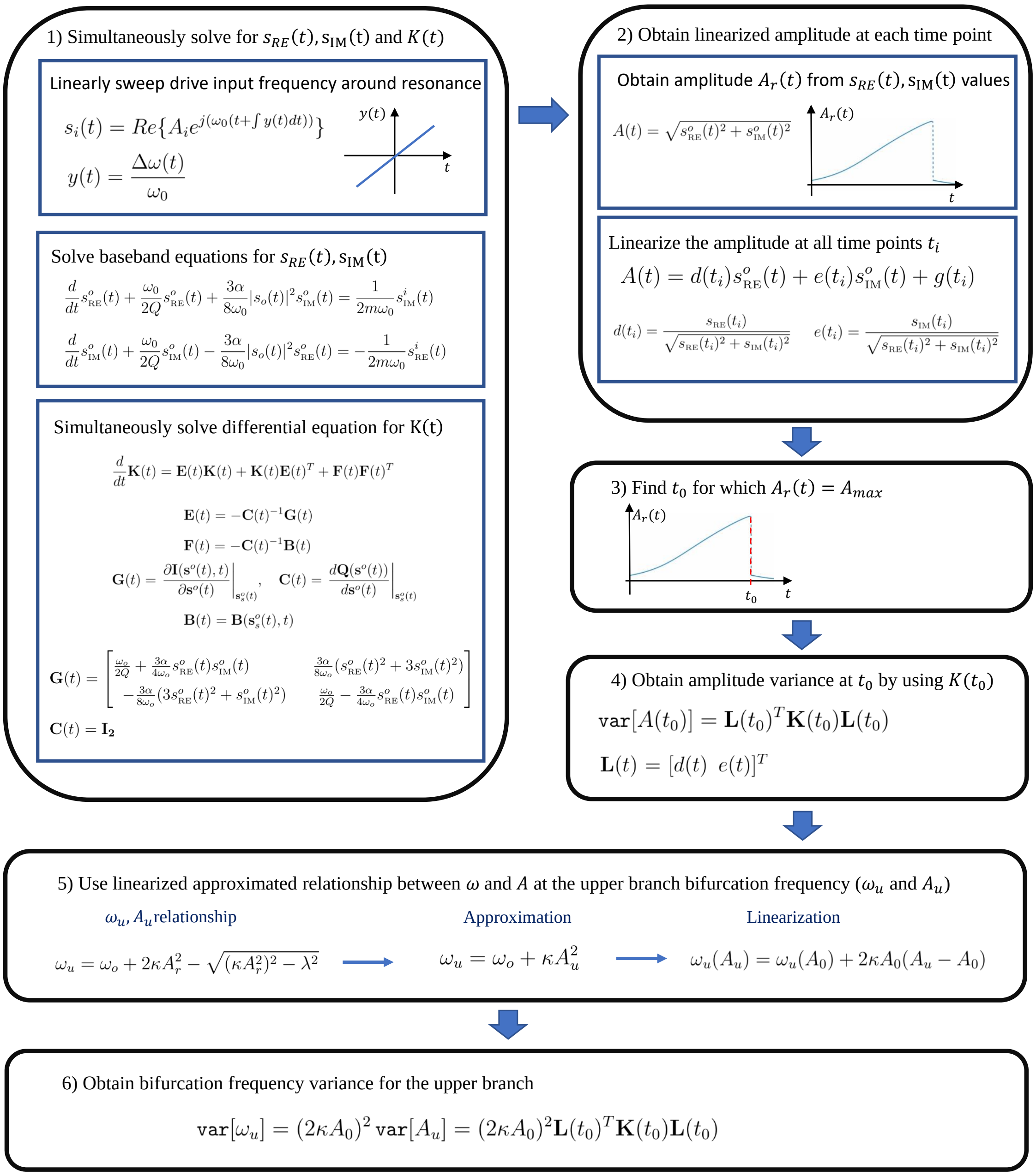

Figure 2.3: Flowchart of the procedure of obtaining the bifurcation frequency variance for the upper branch of the resonator operating in the nonlinear regime via the non-Monte Carlo method

We record the numerically identified maximum amplitude in this noiseless sweep as the mean value A_u^m and the corresponding covariance matrix $\mathbf{K}(t_0)$ at that point in order to quantify the variation around this mean. We use $\mathbf{K}(t_0)$ to obtain the variance of A_u, and convert it to the variance of f_u using Eqn. (1.12). This procedure

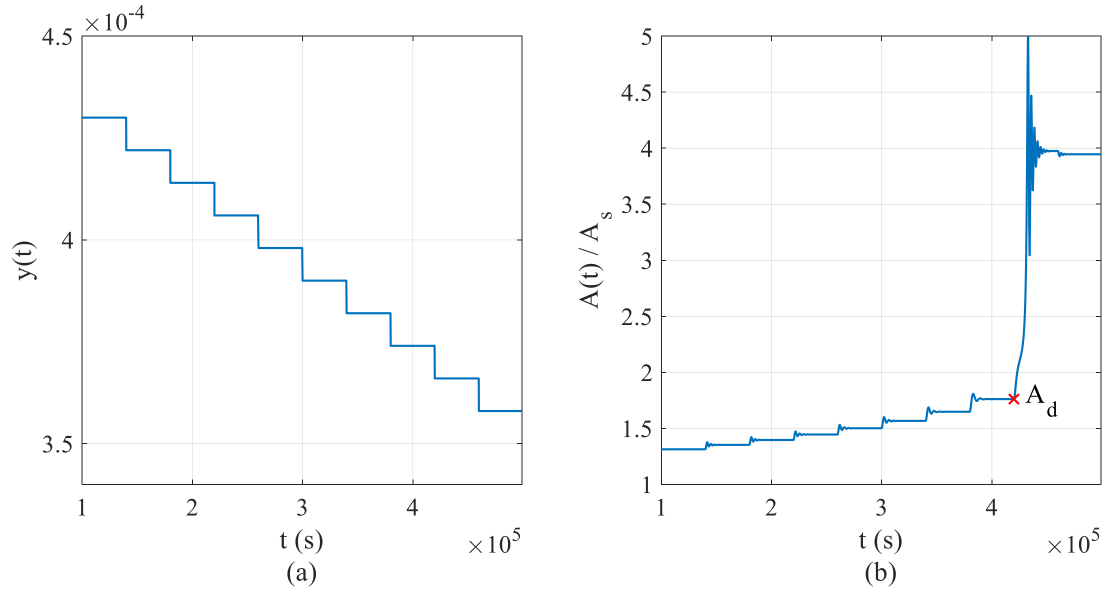

Figure 2.4: The staircase fractional frequency input (a) and the resulting output amplitude (b) for the backward frequency sweep.

is illustrated in detail in the flowchart in Figure 2.3.

To obtain the variance of the bifurcation frequency in the lower branch (f_d) of the nonlinear resonator response, we employ a procedure similar to the one above. We first perform a linear high-to-low (backward) noiseless sweep of frequency in order to obtain the 5-4-2-1 curve in Figure 1.1.c. Theoretically, f_d corresponds to the point at which the amplitude gradient is infinite. However, as in the case of A_u, numerical gradient information is not reliable, and an alternative way to obtain the motion amplitude A_d at f_d is needed. As can be seen in Figure 2.1 (the curve for the backward sweep), the jump does not occur instantaneously in the numerical sweep, but is rather a continuous but quickly increasing signal. In contrast with the case for A_u, where there is a point which closely approximates it and can be computed reliably (A_{max}), there exists no such point in the lower branch. In this case, the computation of the exact value for A_d in a linear sweep proves impossible to obtain reliably. To this end, we devise a two-sweep method to obtain the variance in f_d. First, we perform a variation of the linear sweep, wherein we do not linearly sweep the frequency but instead we decrement it step by step in the form of a staircase function, as shown in Figure 2.4.a. The variable $y(t)$ stands for the fractional frequency deviation, defined as $y(t) = \frac{\Delta\omega(t)}{\omega_o}$. In this setup, after each decrement we wait for the output values to settle before moving down a step. This enables us to acquire a very close estimate of the jump point, where we can identify A_d, which is defined as the amplitude of the signal just before the jump in the output. A plot of the output amplitude in this setup and the estimated A_d value are shown in Figure 2.4.b. Note that the output amplitude is normalized via a normalization constant A_s, which is defined as the output amplitude of the system at the spinodal point. The accuracy of the estimation is of course dependent on the resolution of our staircase signal. We make sure that the resolution is high enough so that we get a good approximation for A_d. We record the amplitude at the identified point as the mean A_d^m. Second, we run the linear backward open-loop sweep, and as A_d we pick the point where the output amplitude is the value of A_d we computed in the first staircase sweep. We use $\mathbf{K}(t_0)$ at that same time point during the sweep to compute the variance of A_d, which is finally converted to $\mathtt{var}[f_d]$ using the relationship in Eqn. (1.12). This procedure is illustrated in detail in the flowchart in Figure 2.5. The details are given below.

The amplitude $A(t)$ of the resonator response is given by:

$$A(t) = \sqrt{s_{\mathrm{RE}}^o(t)^2 + s_{\mathrm{IM}}^o(t)^2} \tag{2.58}$$

By using the Taylor series expansion, we linearize $A(t)$ with respect to $s_{\mathrm{RE}}^o(t)$ and $s_{\mathrm{IM}}^o(t)$ around t_0 to obtain:

$$\begin{aligned} A(t) &= d(t_0)s_{\mathrm{RE}}^o(t) + e(t_0)s_{\mathrm{IM}}^o(t) + g(t_0) \\ d(t_0) &= \frac{s_{\mathrm{RE}}(t_0)}{\sqrt{s_{\mathrm{RE}}(t_0)^2 + s_{\mathrm{IM}}(t_0)^2}} \\ e(t_0) &= \frac{s_{\mathrm{IM}}(t_0)}{\sqrt{s_{\mathrm{RE}}(t_0)^2 + s_{\mathrm{IM}}(t_0)^2}} \end{aligned} \tag{2.59}$$

where $d(t_0)$ and $e(t_0)$ are the constant weights for the real and imaginary parts, respectively, and $g(t_0)$ represents all of the deterministic terms, which are irrelevant in a variance computation.

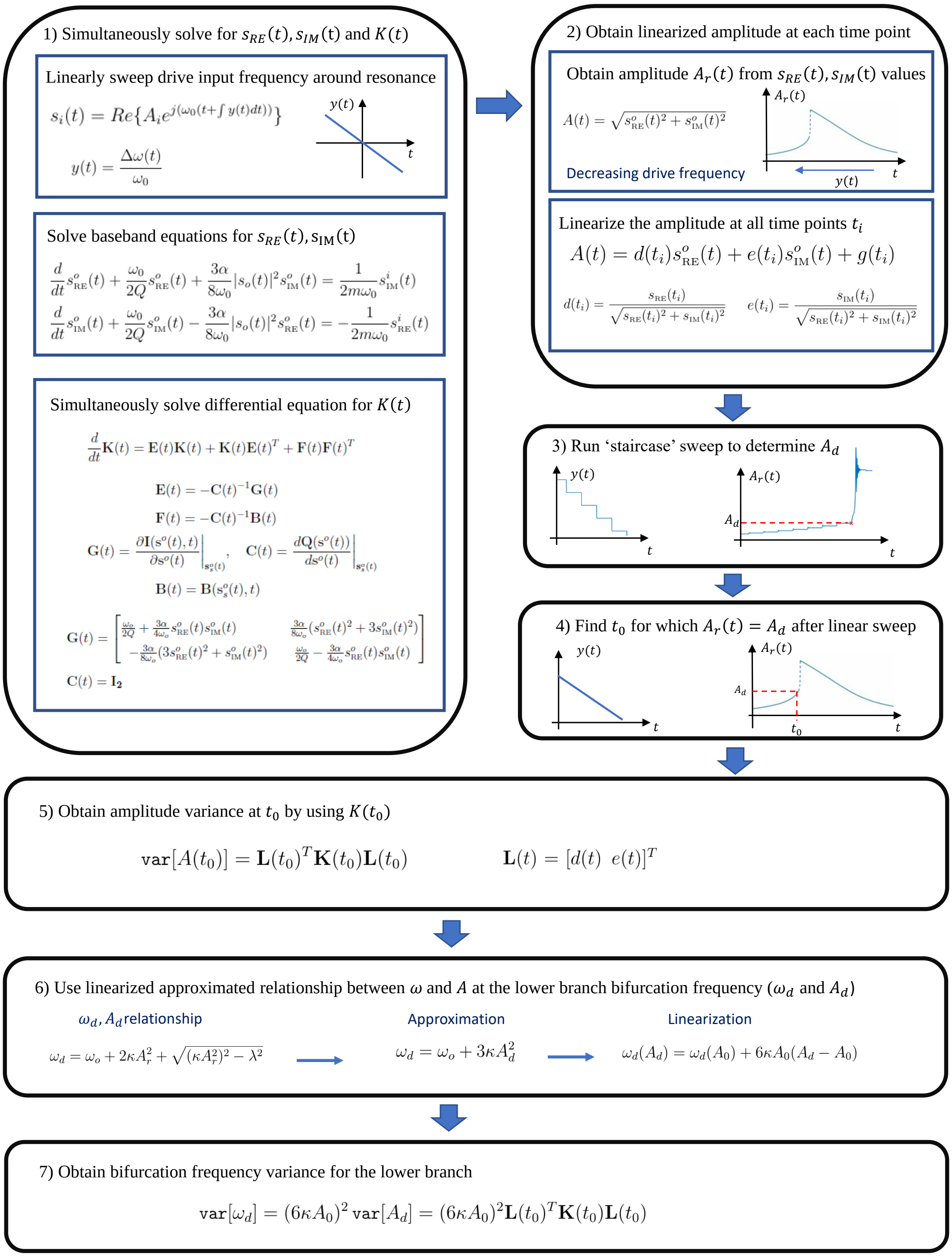

Figure 2.5: Flowchart of the procedure of obtaining the bifurcation frequency variance for the lower branch of the resonator operating in the nonlinear regime via the non-Monte Carlo method

We define the vector $\mathbf{L}(t) = [d(t)\ \ e(t)]^T$, and compute $\texttt{var}[A(t_0)]$ with

$$\texttt{var}[A(t_0)] = \mathbf{L}(t_0)^T \mathbf{K}(t_0) \mathbf{L}(t_0) \tag{2.60}$$

where t_0 is the point corresponding to the bifurcation frequency inputs identified as described above. It corresponds to the pairs A_u, f_u or A_d, f_d in the response.

In order to convert $\texttt{var}[A(t_0)]$ (that gives us $\texttt{var}[A_u]$ and $\texttt{var}[A_d]$) into the variances of f_u and f_d, we use the following procedure. When operating far from the spinodal point, *i.e.,* at much larger drives than the one at the onset of hysteresis, the relationships between bifurcation frequencies and motion amplitudes in Eqns. (1.12) [Landau and Lifshitz, 1976] in the background section can be approximated as [Maillet et al., 2018]:

$$\begin{aligned} \omega_u &= \omega_o + \kappa A_u^2 \\ \omega_d &= \omega_o + 3\kappa A_d^2 \end{aligned} \tag{2.61}$$

In order to compute the variances for f_u and f_d, we linearize the quadratic functions above around a point A_0 to obtain:

$$f_u(A_u) = f_u(A_0) + \tfrac{\kappa}{\pi} A_0 (A_u - A_0) \tag{2.62}$$

for f_u, similarly for f_d. Here, $A_0 = A_u^m$ and $A_0 = A_d^m$ are used, which were recorded at the identified points in the noiseless sweeps as described above. Finally, we compute:

$$\texttt{var}[f_u] = (\tfrac{\kappa}{\pi} A_u^m)^2 \, \texttt{var}[A_u] \tag{2.63}$$

$$\texttt{var}[f_d] = (\tfrac{3\kappa}{\pi} A_d^m)^2 \, \texttt{var}[A_d] \tag{2.64}$$

Chapter 3

VALIDATION OF THE METHOD AND APPROXIMATIONS

3.1 Validating the First-Order Baseband Approximation

To verify that the first-order baseband equation for the Duffing oscillator is a good approximation to the original passband equation, we compare their frequency responses. We first validate the deterministic resonator model (without noise), and then we perform stochastic simulations to compare the models with noise.

3.1.1 Verifying the Deterministic Baseband Model

To compare the deterministic models, we numerically obtain magnitude and phase responses for the resonator operating in the linear and nonlinear regimes, and compute the relative error between the two models (passband and baseband) as a comparison metric. For the linear resonator (with nonlinear coefficient $\alpha = 0$), theoretical comparison is also included, since the transfer functions for both models can be used to obtain the frequency responses.

Comparing the Transfer Functions

For the resonator operating in the linear regime, we can directly use the transfer functions of the first-order baseband and the second-order passband system to compare their magnitude and phase respones theoretically. The transfer functions, named as $H_{PB}(\omega)$ (passband) and $H_{BB}(\omega)$ (baseband) for both are as follows

$$H_{PB}(\omega) = \frac{1}{m} \frac{1}{(-\omega^2 + j\frac{\omega_o}{Q}\omega + \omega_o^2)} \tag{3.1}$$

$$H_{BB}(\omega) = \frac{1}{j2m\omega_o} \frac{1}{(j\omega + \frac{\omega_o}{2Q})} \tag{3.2}$$

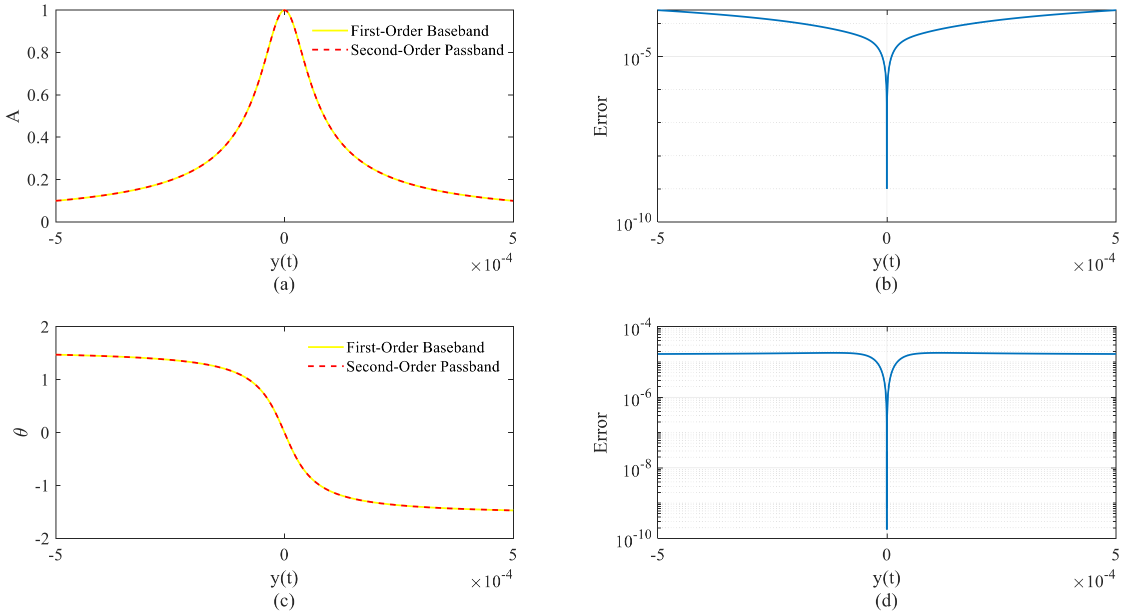

Figure 3.1: Theoretically obtained magnitude (a) and phase (c) responses of the first-order baseband and second-order passband models and their respective relative errors (b), (d)

To compare them, the error metric (E) shown in Eqn. (3.3) was used:

$$E = \frac{|X_{PB} - X_{BB}|}{|X_{PB}|} \tag{3.3}$$

where X_{PB} and X_{BB} represent the passband and baseband quantities, respectively. The magnitude and phase responses and their errors (calculated via Eqn. (3.3)) are shown in Figure 3.1 above. As can be observed from the figure, the relative error is never greater than 10^{-3}, which is an indicator of a good approximation in theory.

Comparing Numerical Solutions

Since our method relies on the numerical solution of the baseband equation, a comparison between the numerical solutions of both models needs to be performed. Numerical solutions to both the first-order baseband and second-order passband deterministic models of the Duffing resonator are obtained and compared to see if the approximation is accurate.

The deterministic baseband resonator is described by the nonlinear first-order

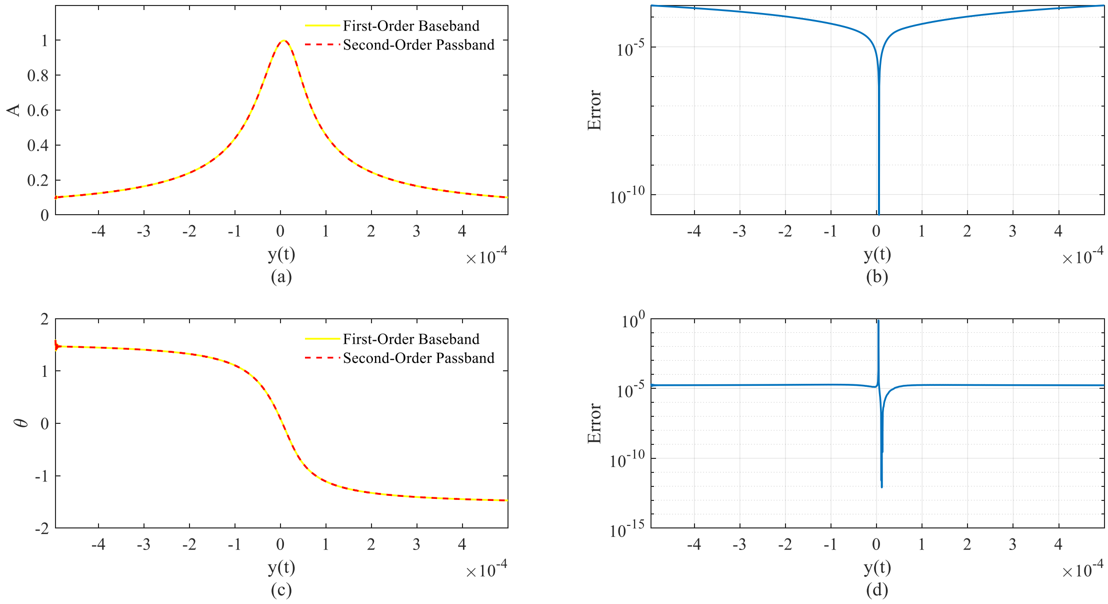

Figure 3.2: Numerically obtained magnitude (a) and phase (c) responses of the linear first-order baseband and second-order passband models and their respective relative errors (b), (d)

complex differential equation in Eqn. (2.25). In order to solve it numerically, the equation has to be in real form. So, by separating its real and imaginary parts into two equations, we get two differential equations as in Eqns. (2.43) and (2.44) (without noise) that describe the system. This system of two coupled differential equations for the real and imaginary parts of the output is used in the implementation of the numerical solution for the baseband model.

The equations describing the first-order baseband system were solved using the 4^{th} order Runge-Kutta method for numerical integration [Süli and Mayers, 2003]. Then, its results were compared with the passband system equation solution, obtained via the same numerical method. The magnitude and phase plots of the baseband system were compared to the passband plots.

The procedure is as follows. The baseband system is driven with a baseband signal of the form

$$s_i^b(t) = A_i e^{j\omega_0 \int y(t)dt} \tag{3.4}$$

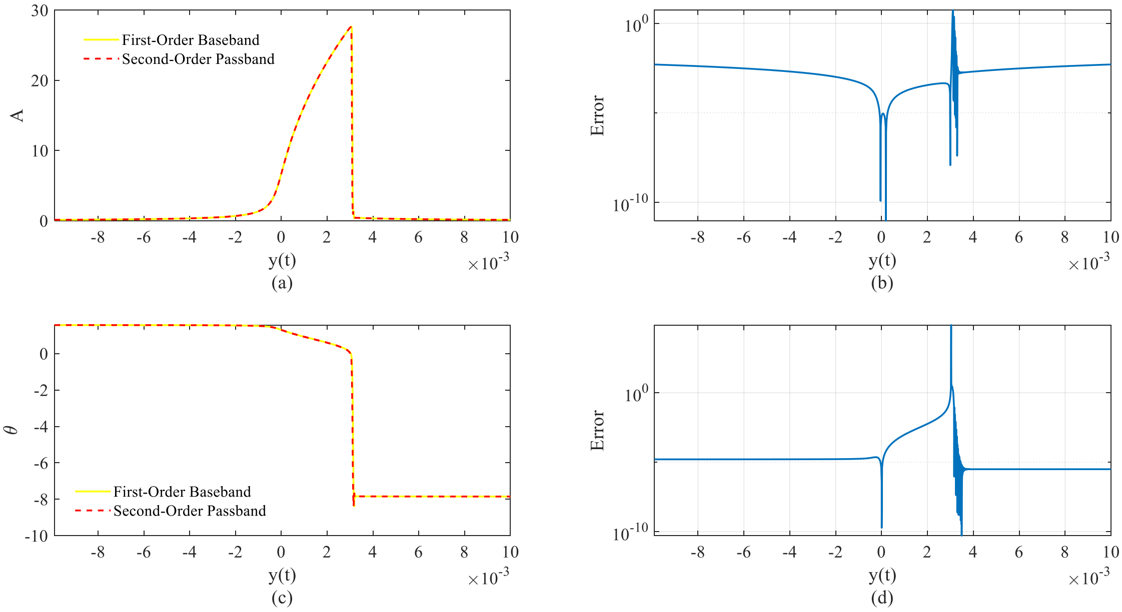

Figure 3.3: Magnitude (a) and phase (c) responses of the first-order baseband and second-order passband nonlinear models with forward frequency sweep and their respective relative errors (b), (d)

where A_i is the drive amplitude. The passband system is driven with the real part of its high frequency version

$$s_i(t) = Re\{A_i e^{j(\omega_0(t+\int y(t)dt))}\} \tag{3.5}$$

The signal $y(t)$ is known as the fractional frequency deviation:

$$y(t) = \frac{\Delta\omega(t)}{\omega_0} \tag{3.6}$$

and for this simulation we use a linear function for $y(t)$ to sweep around the resonance frequency.

This procedure is repeated three times, once for the resonator operating in the linear regime, and twice for the nonlinear resonator. As mentioned above, the resonator in the nonlinear regime can have two stable states, which appear depending on how the drive frequency is swept. If a forward sweep is performed, we observe the upper branch of the resonator response. In the backward sweep, the lower branch of the resonator response is observed. Therefore, both of these responses were obtained separately.

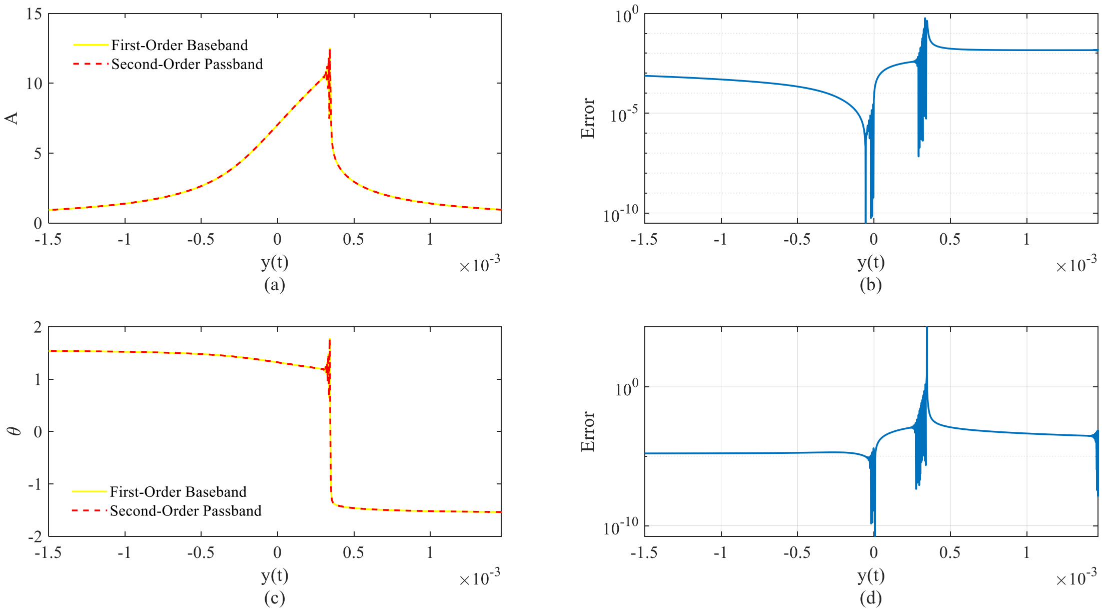

Figure 3.4: Numerically obtained magnitude (a) and phase (c) responses of the first-order baseband and second-order passband nonlinear models with backward frequency sweep and their respective relative errors (b), (d)

The results are plotted in Figures 3.2, 3.3 and 3.4. The obtained relative errors show that the first-order baseband model is an accurate approximation of the second-order passband model. However, there is bound to be some inevitable error, especially at the bifurcation frequencies. In the following section, we investigate if these errors in the deterministic approximation affect the stochastic results of the models.

3.1.2 Verifying the Stochastic Baseband Model

Having confirmed the validity of the deterministic baseband model in the linear and nonlinear regime, we move on to the stochastic model.

Stochastic simulations of both the passband and baseband open-loop resonator were performed to verify that our first-order baseband approximation holds. The passband model is based on a detailed second-order high-frequency model of all the system components of the open-loop system with no approximations. The baseband model is the first-order low-frequency approximation we present in Chapter 2 in

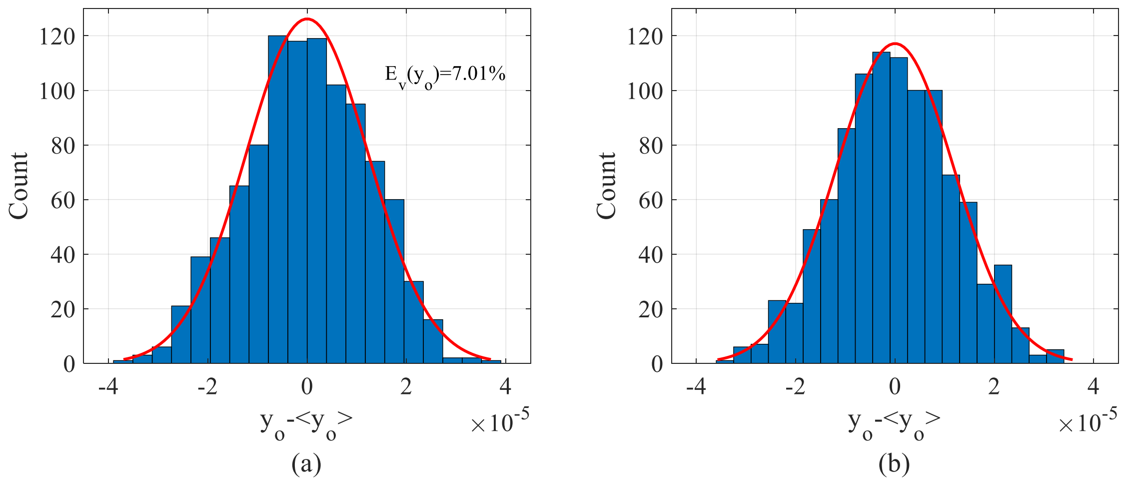

Figure 3.5: Histograms for the resonance frequency obtained using data obtained via the baseband (a) and passband (b) stochastic models

Eqn. (2.25). A random number generator is used to introduce the thermomechanical noise of the resonator. The time-step and numerical method are chosen carefully so that the results obtained are accurate. The numerical results for the stochastic system are obtained via MATLAB®Simulink® [The MathWorks, Inc., 2020].

All of the results we report below relate to the *fractional frequency deviation* $y(t)$, defined as $y(t) = \frac{\Delta f(t)}{f^m}$, where Δf represents the frequency fluctuation and f^m is the mean value. For the three characteristic frequencies of interest, we define the following accordingly: $y_o(t) = \frac{\Delta f_o(t)}{f_o^m}$, $y_u(t) = \frac{\Delta f_u(t)}{f_u^m}$ and $y_d(t) = \frac{\Delta f_d(t)}{f_d^m}$.

Methodology for the Linear Regime

For the linear model, for each realization, a linear frequency sweep of the input around the resonance frequency is performed. The input signal has the form shown in Eqns. (3.4) and (3.5) for the baseband and passband models, respectively. Each time, the point where the output phase crosses zero is found numerically, and the drive frequency at that value, *i.e.*, the resonance frequency for that realization, is recorded. We recall that we add a $-\frac{\pi}{2}$ shift to the phase before computing this value. This procedure is repeated one thousand times and the ensemble distribution of the resonance frequency is obtained.

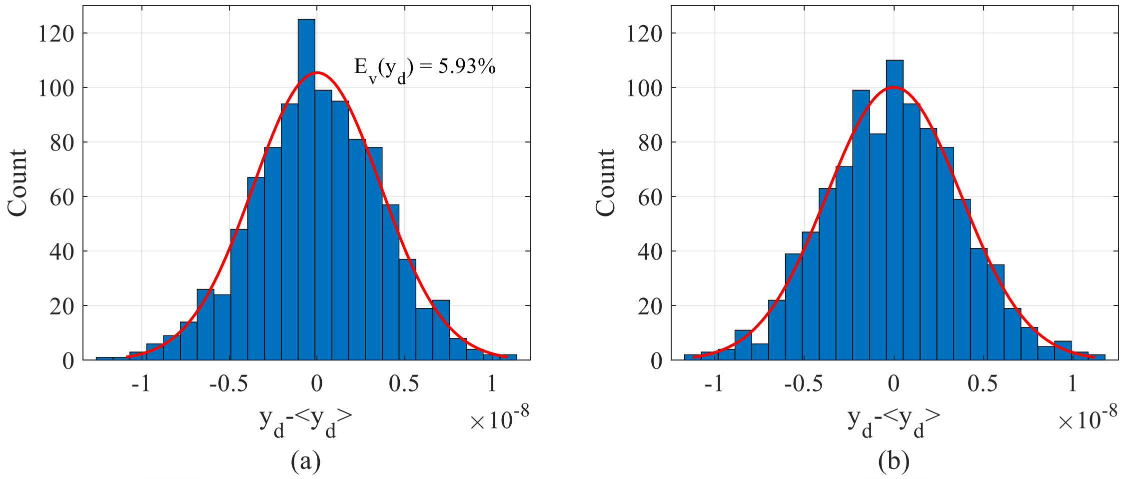

Figure 3.6: Histograms for the f_d bifurcation frequency obtained using data obtained via the baseband (a) and passband (b) stochastic models

Methodology for the Nonlinear Regime

For the f_d variance estimation, a linear frequency sweep from high to low frequencies is performed in the region containing f_d. For each realization, the point where the numerical amplitude gradient has value one is obtained numerically and the drive frequency at that point, *i.e.*, f_d for that realization, is recorded. Again, one thousand realizations are performed and the ensemble distribution of f_d is obtained for both the passband and baseband models.

For the f_u variance estimation, a low to high linear frequency sweep is performed in the region containing f_u. For each realization, the point where the amplitude maximum is located is found and the drive frequency at that point is recorded, corresponding to f_u for that realization. Finally, the ensemble distribution of f_u is obtained using one thousand realizations for both the baseband and passband models.

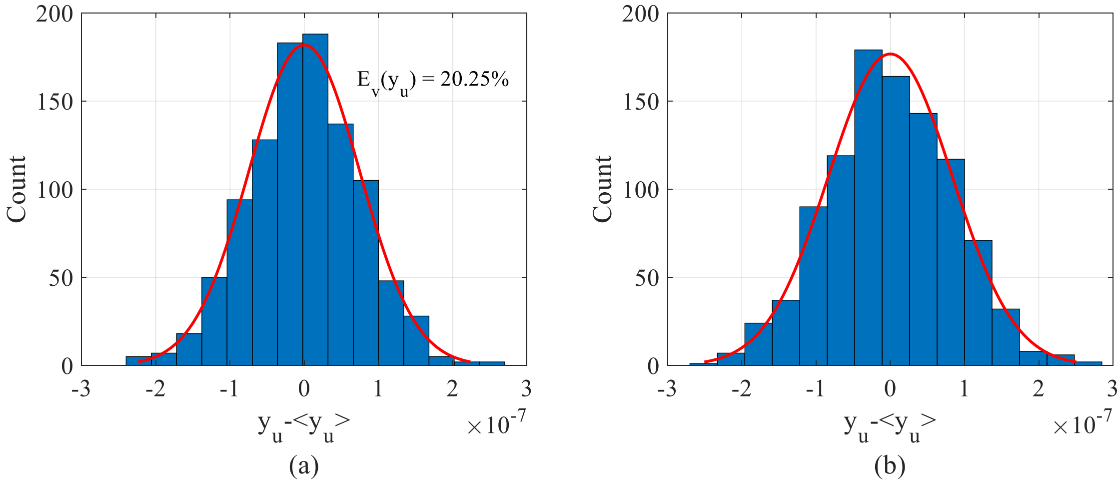

Figure 3.7: Histograms for the f_u bifurcation frequency obtained using data obtained via the baseband (a) and passband (b) stochastic models

Results

The histograms for both the passband and baseband models are obtained and compared. The relative error in variance is defined as:

$$E_v = \frac{|var(f^{BB}) - var(f^{PB})|}{var(f^{PB})} \tag{3.7}$$

where $\cdot^{BB}$ and $\cdot^{PB}$ denote the baseband and passband frequencies, respectively. We use this error metric to quantify the difference between the two models.

The results for the linear stochastic simulations are shown in Figures 3.5.a and 3.5.b.

The histograms, the variances and the error in variance estimation for the non-linear backward sweep case are shown in Figures 3.6.a and 3.6.b.

The histograms, the variances and the error in variance estimation for the non-linear forward sweep case are shown in Figures 3.7.a and 3.7.b.

These results show that the stochastic behavior of the baseband model closely resembles that of the passband model. In addition, for each of these simulations, the run time of the baseband model is at least ~ 20 times faster than that of the passband model.

Thus, we can conclude that the first-order baseband model accurately approximates the second-order passband model, while reducing the computation time drastically.

3.2 Verification of the non-Monte Carlo Method via Monte Carlo Simulations

To validate the results of our proposed non-Monte Carlo method, we compare them with the ones obtained from extensive Monte Carlo simulations of the baseband resonator model. This comparison aims to validate the approximations employed in deriving the non-Monte Carlo technique, and to ascertain their accuracy. The non-Monte Carlo technique employs the following approximations:

i The covariance equation in (2.47) was derived based on a small noise expansion [Demir and Sangiovanni-Vincentelli, 1998].

ii The phase and amplitude variances were obtained using linearizations of the nonlinear phase and amplitude expressions in terms of the real and imaginary parts as shown in Eqns. (2.51) and (2.59), respectively.

iii The frequency variances were obtained with the further linearizations in Eqns. (2.56) and (2.62).

However, when comparing the MC simulations with the non-MC method results, we have to take into account the shortcomings of the MC method as well. The limitations of the MC technique also add to the existing error between the two methods. Some sources of error arising from the nature of the MC method are summarized below:

i Due to their high computational cost, MC simulations are run for a finite and relatively small number of realizations. As a result, an estimation error in the variance and standard deviation values obtained by the MC method is always present due to finite sample size.

ii The use of a frequency sweep speed that is large enough (so that Monte Carlo simulations do not become prohibitively expensive) results in some additional error. In the sections below we show how the sweep speed affects the accuracy of the obtained standard deviation values with the Monte Carlo method.

3.2.1 Verification for the Linear Regime

The variation of interest for the resonator operating in the linear regime is the standard deviation of the resonance frequency. However, as mentioned in the introduction of Section 3.2, many approximations are employed in the implementation of the non-Monte Carlo technique. Therefore, it is important to know how much information is lost during each approximation step. To observe all the steps of the computation, we will first be investigating the system outputs: the real and imaginary parts of the resonator displacement $s_o^b(t)$. Their standard deviations are obtained via both methods and compared. Afterwards, the variations in amplitude and phase are compared and the effect of the approximations is examined. Finally, the resonance frequency standard deviations as the values of interest are obtained and the validity of the method as a whole is discussed.

The following relative error metric is employed to quantify the difference in standard deviation estimation between the two methods:

$$E_\sigma = \frac{\left|\sigma[X]^{\mathrm{M}} - \sigma[X]^{\mathrm{N}}\right|}{\sigma[X]^{\mathrm{N}}} \tag{3.8}$$

where $\sigma[\cdot]$ denotes the standard deviation operator, X denotes the signal of interest and the superscripts $\cdot^{\mathrm{M}}$ and $\cdot^{\mathrm{N}}$ indicate the MC and non-MC method outcomes, respectively.

Variation in Real and Imaginary Parts

First, we compare the standard deviations of the real and imaginary parts of $s_o^b(t)$ obtained via both methods.

With the non-Monte Carlo technique, the covariance matrix for $\mathbf{s}^o(t)$ (the two dimensional vector $[s^o_{\mathrm{RE}}(t)\;\; s^o_{\mathrm{IM}}(t)]^T$) is obtained from Eqn. (2.47) after performing

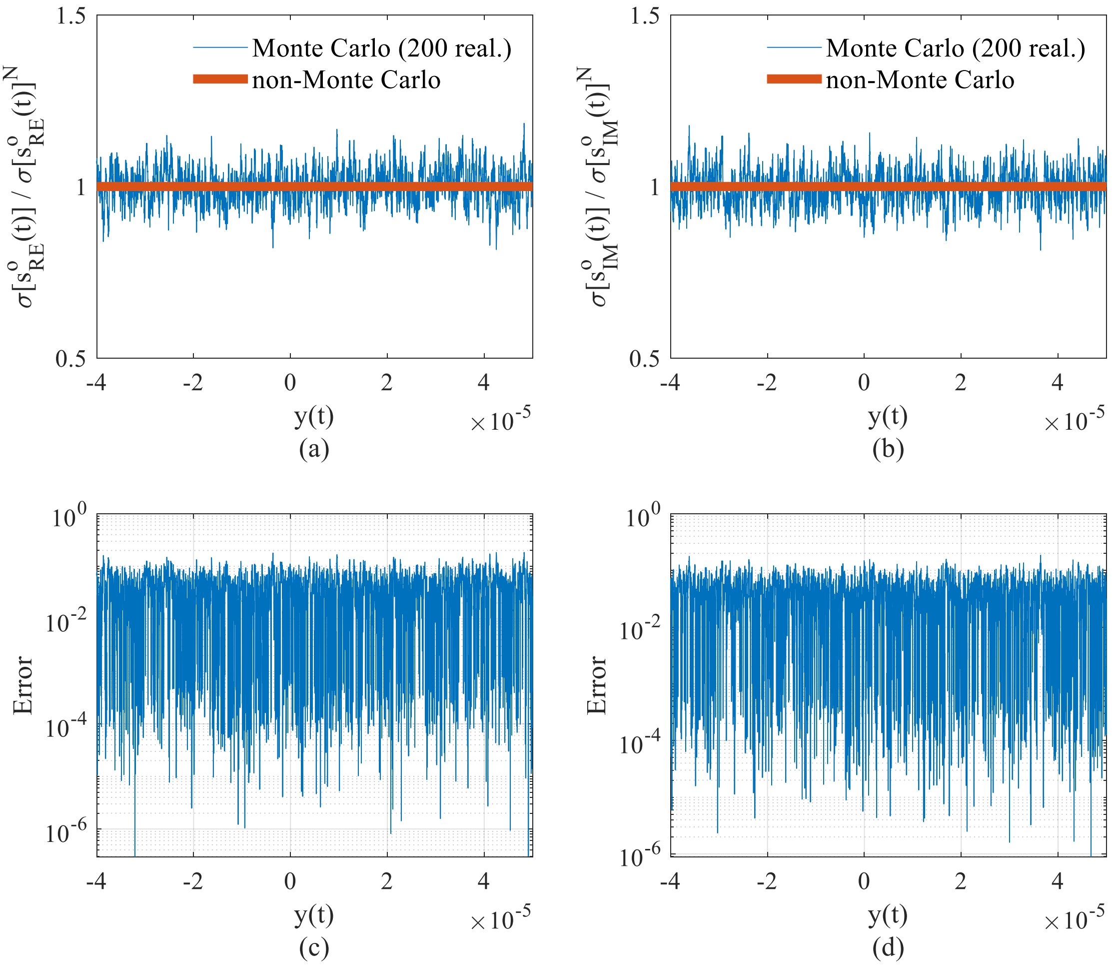

Figure 3.8: Normalized standard deviations of the real (a) and imaginary (b) parts of $s_o^b(t)$ obtained via both the Monte Carlo and non-Monte Carlo methods and their relative errors (c), (d)

a linear sweep of the drive frequency around resonance. Variances for $s^o_{\mathrm{RE}}(t)$ and $s^o_{\mathrm{IM}}(t)$ are obtained from the $\mathbf{K}(t)$ matrix and recorded at each point.

For the Monte Carlo technique, 200 realizations of the same linear sweep, but this time with additive noise generated by a random number generator are performed. The ensemble standard deviations of $s^o_{\mathrm{RE}}(t)$ and $s^o_{\mathrm{IM}}(t)$ at each time point (corresponding to certain drive frequencies) are obtained from the data.

In Figure 3.8.a and 3.8.b, plots of the normalized standard deviations for the real and imaginary parts at all time points during the sweep obtained via both methods

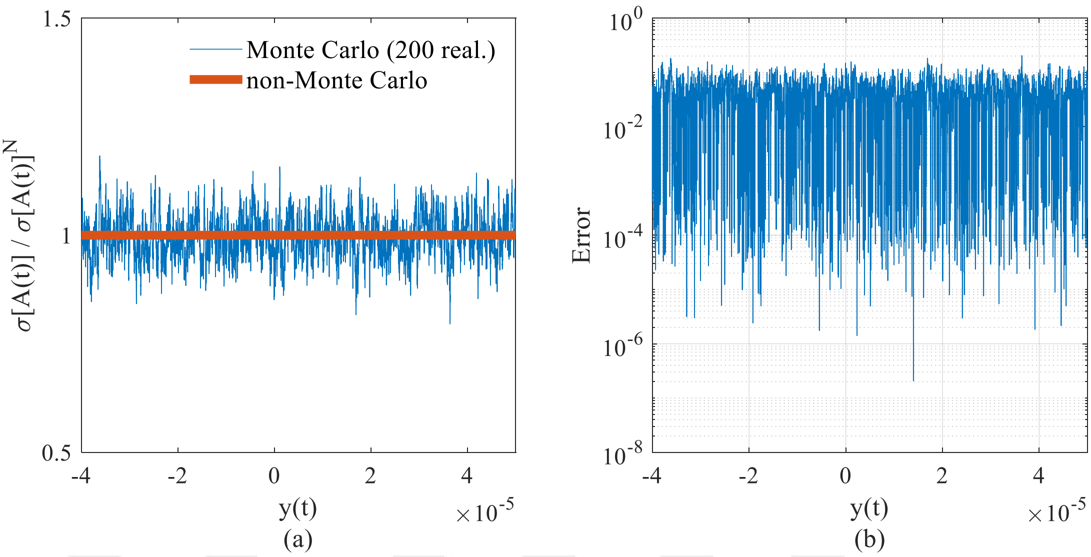

Figure 3.9: Normalized standard deviations of the amplitude (a) of $s_o^b(t)$ obtained via both the Monte Carlo and non-Monte Carlo methods and their relative error (b)

are plotted. The normalization constant is set to be the non-Monte Carlo standard deviation value. As can be observed from these two figures, the two methods are consistent: both observe constant standard deviations over all frequencies, and their values also appear to be a close match.

To quantitatively get a grasp on how compatible these two results are, the errors between the standard deviations obtained by the two methods and calculated using Eqn. (3.8) are plotted in Figures 3.8.c and 3.8.d. It can be observed that the error values fluctuate wildly, but are never above a relative error of 10%, demonstrating the validity of the non-Monte Carlo method for the linear case. The fluctuations arise due to the finite number of realizations for the Monte Carlo method. It is expected that with higher number of realizations, the fluctuations in error will decrease.

Variation in Amplitude and Phase

After obtaining the real and imaginary parts of the output and their standard deviations, we obtain the variation in amplitude and phase of the output with both methods and compare their results.

With the non-Monte Carlo method, the variances for the amplitude and phase

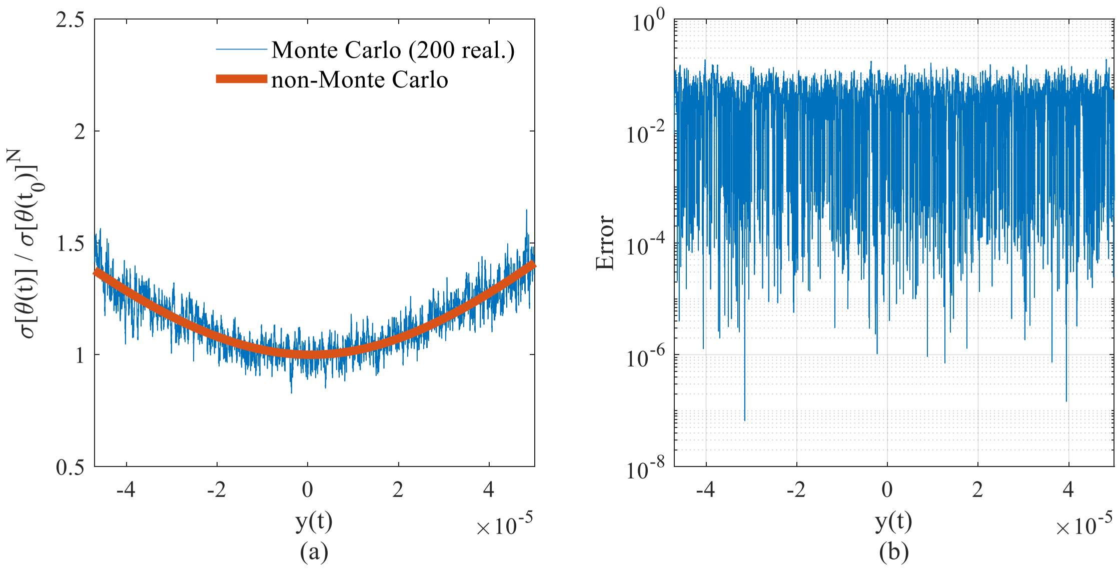

Figure 3.10: Normalized standard deviations of the phase (a) of $s_o^b(t)$ obtained via both the Monte Carlo and non-Monte Carlo methods and their relative error (b)

are obtained from $\mathbf{K}(t)$ by using the linearized expressions for amplitude and phase, giving us the variance expressions for both as shown in Eqns. (2.60) and (2.52), respectively.

With the Monte Carlo method, for each of the realizations, the amplitude and phase values at each time point are obtained by using their equations (without approximating) shown in Eqns. (2.58) and (2.50). The ensemble standard deviations for both the amplitude $A(t)$ and the phase $\theta(t)$ are obtained from the data.

In Figure 3.9.a, the normalized amplitude standard deviations obtained via both methods can be observed. The normalization constant is chosen to be the value of the standard deviation of amplitude obtained by the non-MC method. It can be seen that they are indeed matching, which is proved by the relative error plot in Figure 3.9.b, which shows that the amplitude variation estimation of the non-MC method closely follows the results obtained via the MC method.

In Figure 3.10.a, the normalized phase standard deviations obtained via both methods can be observed. The normalization value is chosen to be the standard deviation of the phase at point t_0, *i.e.*, the point where the drive frequency is equal to resonance. As can be seen from this plot, different from the case of amplitude, the standard deviation in the phase is not constant for all frequencies. It is lowest at the resonance frequency, and increases symmetrically in each direction. Both methods were able to predict this behavior, and their results appear to be in agreement. In Figure 3.10.b, a plot of the relative error between these two methods is shown. The error rarely ever crosses 10%, and is an indicator of a good match between the two.

As can be observed from the obtained results, the approximations employed in obtaining the phase and amplitude variances do not seem to have any drastic effect in the accuracy of the non-MC method. Comparing the relative errors for phase and amplitude with those of the real and imaginary parts (Figure 3.8), we can observe that there is not much difference between the two, and that the approximations in phase and amplitude do not drastically affect the accuracy of the non-MC technique.

Variation in Resonance Frequency

The final step of the noise characterization procedure for the linear resonator is acquiring the standard deviation in resonance frequency.

In the non-MC technique, we derive the resonance frequency variation from the phase variance by using Eqn. (2.57).

In the MC technique, the resonance frequency variance is obtained as explained in Section 3.1.2. For each realization, the stochastic resonance frequency value is recorded, and its standard deviation is obtained from the data recorded from each realization.

Since the resonance frequency variance is obtained directly from the phase variance, we check the standard deviation in phase exactly at the point where it crosses zero, *i.e.,* at resonance. In Figure 3.11.a, the normalized MC phase standard deviation versus number of realizations is shown next to the constant non-MC method value (which is used as the normalization constant). In Figure 3.11.b, their relative error is shown. After 3000 realizations, the error in estimation is about 3.5%, indicating a good match between the results of the two methods.

Finally, we examine the resonance frequency variation. In Figure 3.11.c the frac-

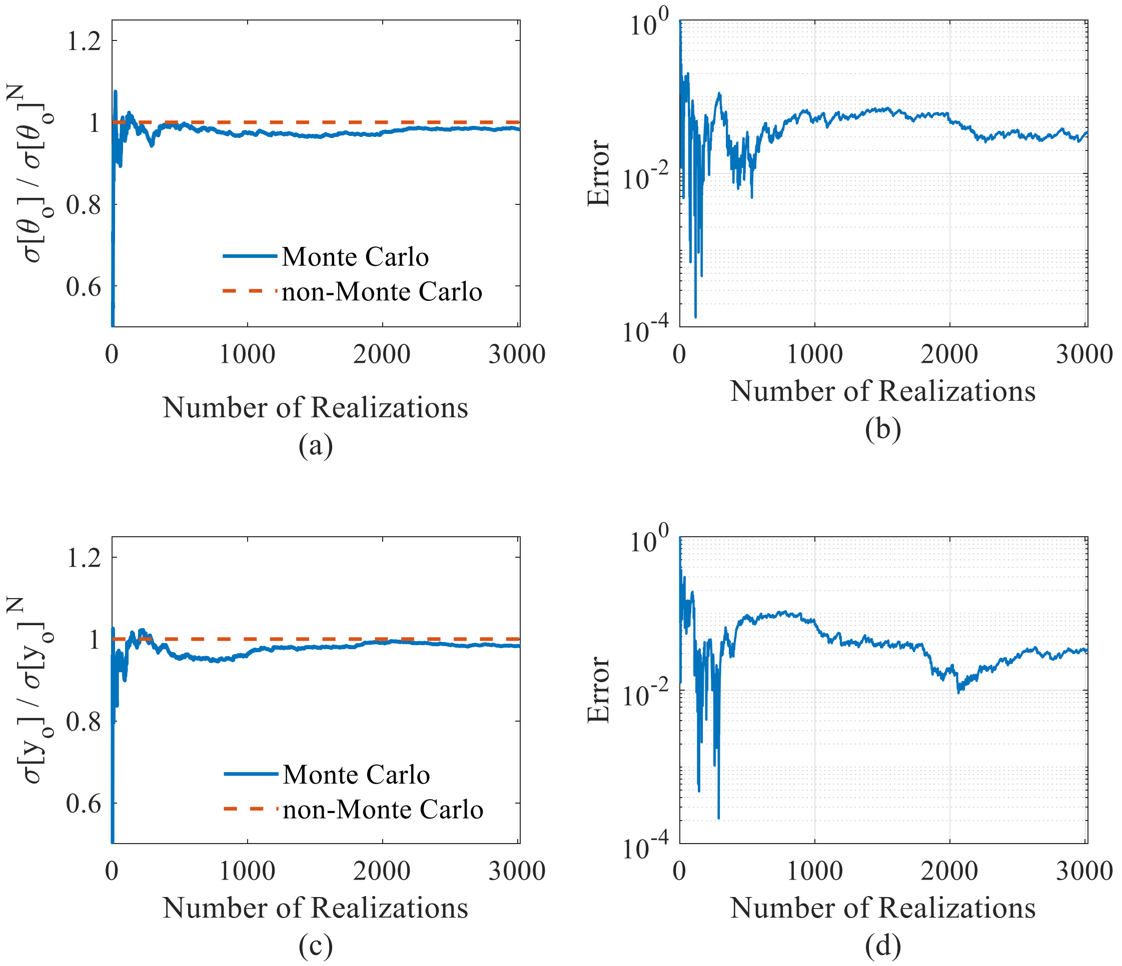

Figure 3.11: Normalized phase response (a) fractional resonance frequency (c) standard deviations for the Monte Carlo and non-Monte Carlo methods versus number of Monte Carlo realizations, and their errors (b), (d)

tional resonance frequency standard deviations obtained via both methods versus number of MC realizations are shown. The results are normalized using the resonance frequency variance obtained via the non-MC method. Their relative error is plotted in Figure 3.11.d. After 3000 realizations, the error in fractional resonance frequency standard deviation estimation is about 3.3%.

These results clearly demonstrate that the non-MC method is in close agreement with the MC results, rendering it a valid technique to obtain the resonance frequency variance for linear resonators.

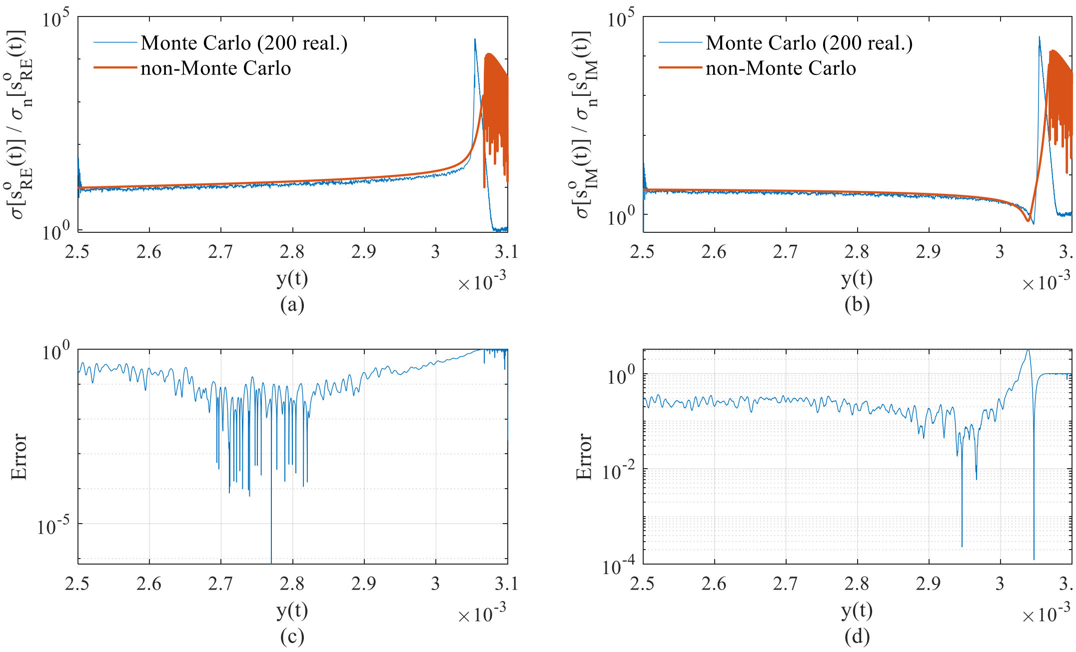

Figure 3.12: Normalized standard deviations of the real (a) and imaginary (b) parts of $s_o^b(t)$ for the forward sweep obtained via both the Monte Carlo and non-Monte Carlo methods and their relative errors (c), (d)

3.2.2 Verification for the Nonlinear Regime

For the resonator operating in the nonlinear regime, the variations of interest are the standard deviations of the bifurcation frequencies. For the upper branch, that is the standard deviation in the fractional frequency y_u, while for the lower branch it is the standard deviation in y_d. Similar to the linear case, the variation in the bifurcation frequencies is not observed and analyzed directly. Instead, we take a step by step approach where we analyze the fluctuations in the quantities obtained in the intermediate steps to ascertain how accurate our approximations are. First we investigate the system outputs: the real and imaginary parts of the resonator displacement $s_o^b(t)$. Their standard deviations are obtained via both methods and compared. Second, the variations in amplitude are compared and the effect of the approximations is examined. Finally, the bifurcation frequency standard deviations as the values of interest are obtained and the validity of the method as a whole is discussed.

The relative error metric in Eqn. (3.8) is employed to quantify the difference in standard deviation estimation between the two methods. All standard deviation values are normalized with respect to a reference value for easy comparison. This reference value is chosen to be the standard deviation of the respective quantities obtained at resonance when the system is driven with half the spinodal drive amplitude in the linear regime. We shall denote the normalization standard deviation values for the quantities of interest as $\sigma_n[\cdot]$. In cases where a constant value is being compared, the normalization value is chosen to be the standard deviation obtained via the non-Monte Carlo method, denoted as $\sigma[\cdot]^N$.

Variation in Real and Imaginary Parts

First, we compare the standard deviations of the real and imaginary parts of $s_o^b(t)$ for the system operating in the nonlinear regime obtained via both methods.

For both the forward and backward sweep, the covariance matrix of $s_o^b(t)$ for the non-MC technique is obtained from Eqn. (2.47) after performing a deterministic linear sweep of the drive frequency. Standard deviations for $s^o_{\text{RE}}(t)$ and $s^o_{\text{IM}}(t)$ are obtained from the $\mathbf{K}(t)$ matrix and recorded at each point.

For the Monte Carlo technique, 200 realizations of the same linear sweep around the frequency of interest (forward sweep for the upper branch, and backward sweep for the lower branch), but this time with additive noise generated by a random number generator are performed. Afterwards, the ensemble standard deviations of $s^o_{\text{RE}}(t)$ and $s^o_{\text{IM}}(t)$ are obtained from the data for both the forward sweep and backward sweep cases.

To quantitatively examine how well the two methods match, the logarithmic plots for the standard deviations of the real and imaginary parts and the errors between them obtained by the two methods are calculated using Eqn. (3.8) and are plotted.

In Figures 3.12 and 3.13, we display the plots for the real and imaginary part standard deviations for the forward and backward frequency sweeps in the nonlinear

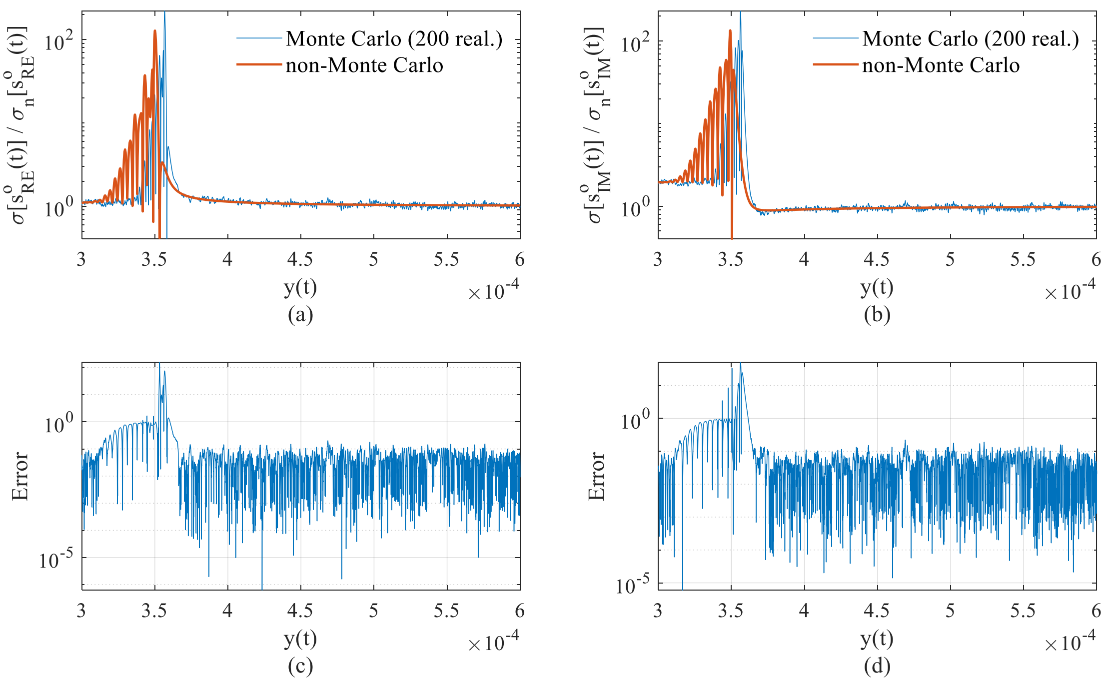

Figure 3.13: Normalized standard deviations of the real (a) and imaginary (b) parts of $s_o^b(t)$ for the backward sweep obtained via both the Monte Carlo and non-Monte Carlo methods and their relative errors (c), (d)

regime. The error plots show that the results from the non-MC technique are in agreement with the MC expected variations. It is worth noting that since this is a numerical simulation, the point at the bifurcation frequency where the amplitude jumps with infinite slope does not appear as such here. Instead, it appears to be a continuous line which increases very fast, as can be seen in Figures 3.12 and 3.13. The slower the frequency sweep, the better that jump point can be observed, as we will show in the sections below.

If we look carefully at figures a and b for both cases, a new interesting phenomenon can be observed. Different from the linear case where both the real and imaginary parts have identical standard deviations (Figure 3.8), in the nonlinear case we observe that there is a difference between the two. As the drive frequency approaches the jump value (in this case y_u or y_d), the variations in the real and imaginary parts move further away from each other, in what can be described as a

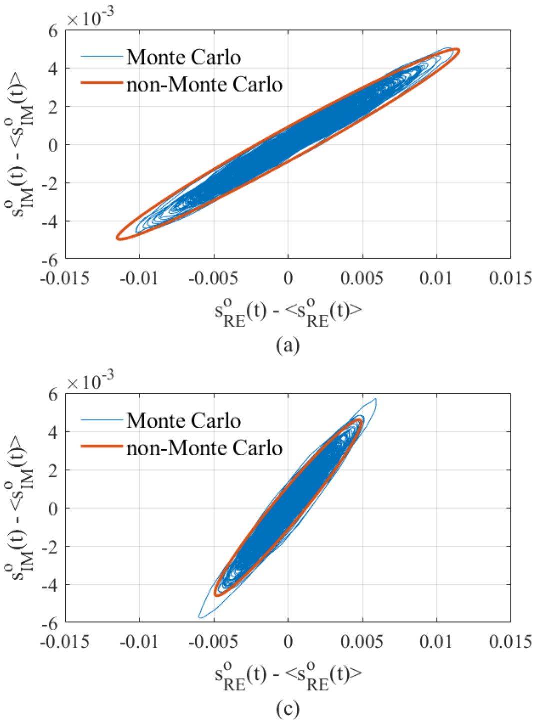

Figure 3.14: Ellipsoids showing the regions for the real and imaginary parts for fixed drive frequencies (fractional) of (a) $y = 2.5x10^{-3}$, (b) $y = 2.3x10^{-3}$, (c) $y = 1.5x10^{-3}$ and (d) $y = 1x10^{-3}$

noise-squeezing effect, which is indeed an existent effect in Duffing resonators, mentioned previously in [Buks and Yurke, 2006]. This effect can be better observed if we plot the confidence intervals for these signals at a certain fixed frequency in the complex plane as shown in Figure 3.14.

The non-MC ellipse for a certain frequency is the 99% confidence interval obtained via the covariance matrix in Eqn. (2.47) evaluated at the time point corresponding to that drive frequency. The MC ellipses are obtained by running the system with a constant frequency and plotting all points obtained (after the outputs have settled and are in steady-state).

These so-called ellipses clearly show this squeezing effect happening in the noise. Different from the linear case, these plots are no longer circular, but they are tilted, which means the real and imaginary parts do not have the same variances. Another effect we notice is that these ellipses are not always the same. They rotate with

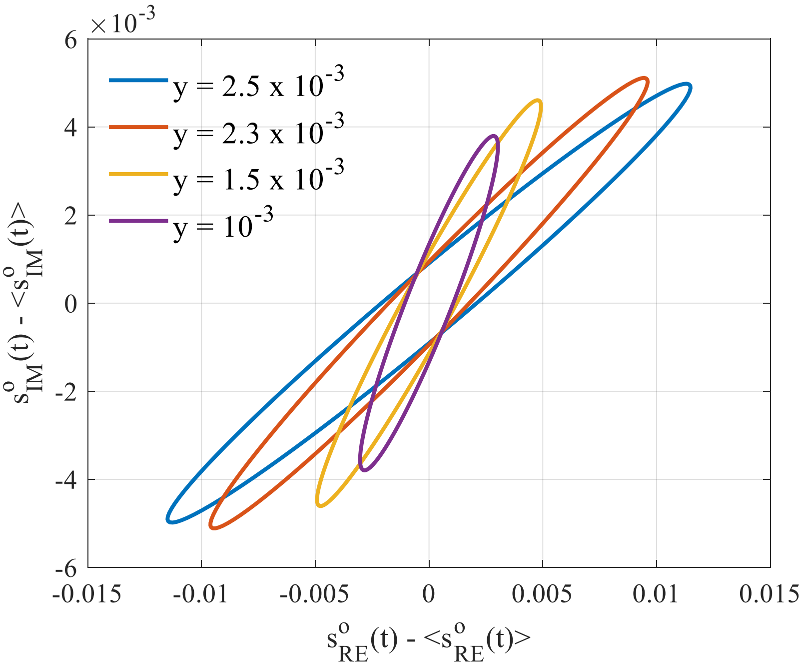

Figure 3.15: Ellipsoids obtained via the non-Monte Carlo method for various driving (fractional) frequencies

change in drive frequency, as can be observed in Figure 3.4. The closer to the bifurcation frequency, the more noticeable this squeezing effect is, displaying that in our case the variation in the imaginary part is much lower than that in the real part.

Variation in Amplitude

In this section we analyze the variation in output amplitude. Since the amplitude standard deviation is the key to obtaining the variation in the bifurcation frequencies, making sure that the non-MC technique accurately estimates the amplitude variance is of utmost importance.

With the non-MC method, the variation in amplitude is obtained from $\mathbf{K}(t)$ by using the linearized expression for amplitude giving us the variance expression as shown in Eqn. (2.60).

With the MC method, for each realization, the amplitude values at each time

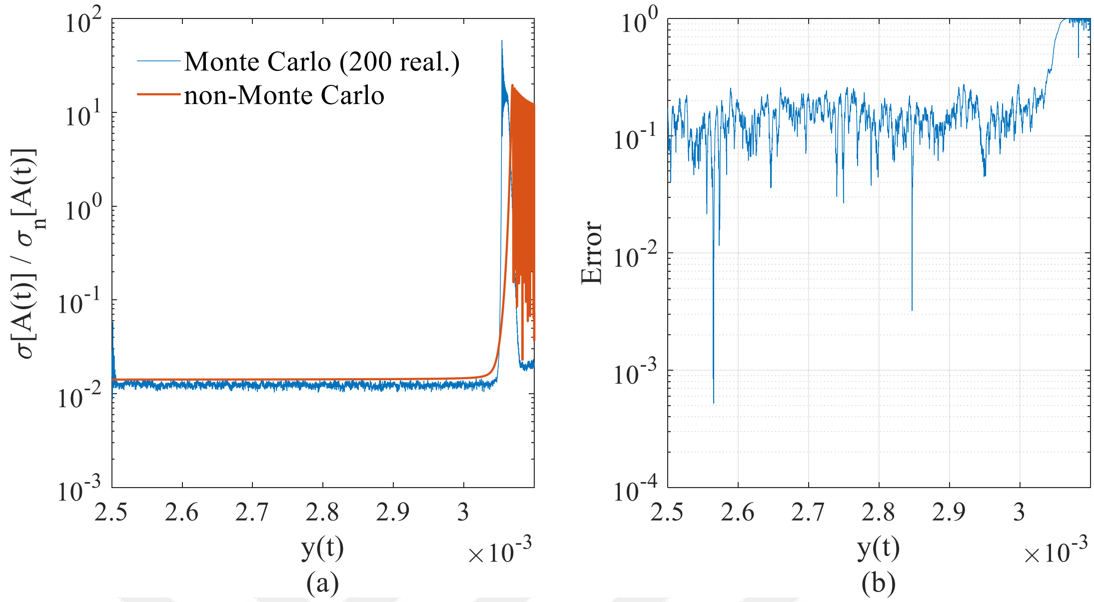

Figure 3.16: Amplitude variance for forward sweep obtained via both methods

(drive frequency) point are obtained by using Eqn. (2.58) (without approximations). The ensemble standard deviation for the resonator amplitude is obtained from the data.

In Figure 3.16 we can see a plot of the amplitude variance from a forward sweep obtained via both methods. The same plot obtained for the backward sweep of the drive frequency is shown in Figure 3.17. The results show that both methods are pretty consistent with each other. Here, we can observe that the squeezing effect for the real and imaginary parts observed in Figure 3.14 is gone, and we have a somewhat constant amplitude variance in the vicinity of the bifurcation frequencies.

Bifurcation Frequency Variance

As a final step, we investigate the variation in the bifurcation frequencies for both the upper and lower branches.

First, we look into the estimation of the bifurcation frequency variance for the upper branch (y_u). For the non-MC technique, the bifurcation frequency variance is obtained by using Eqn. (2.63). In this setup, we define A_u as the point where the deterministic plot of the output amplitude is maximum for the forward frequency

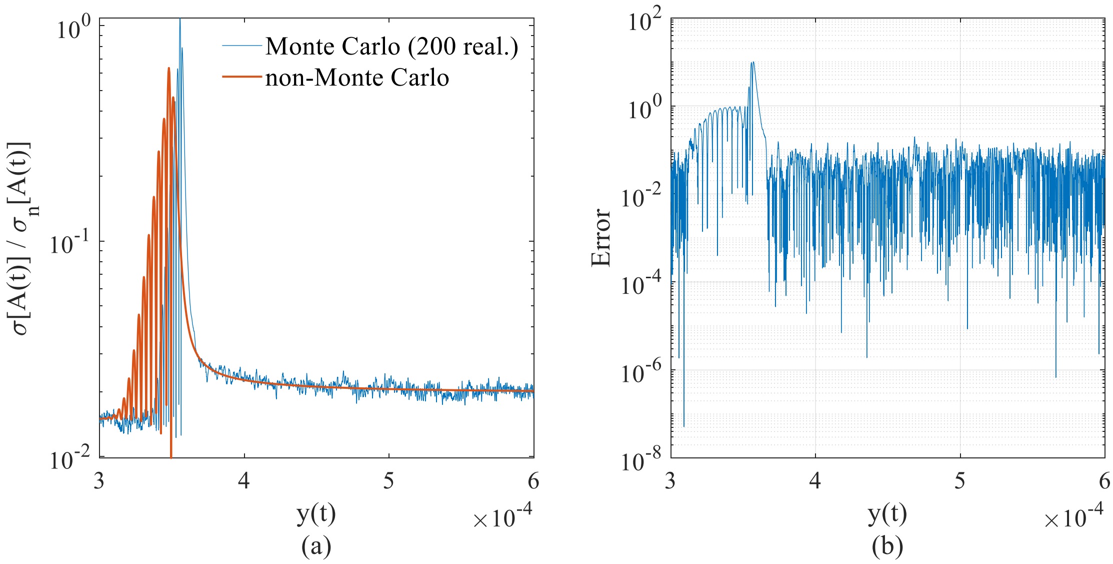

Figure 3.17: Amplitude variance for backward sweep obtained via both methods

sweep. For the MC technique, 200 realizations of the system with noise emulated by a random number generator are run. For the forward sweep, in each realization the point where the amplitude is equal to the deterministic maximum amplitude is obtained and the drive frequency corresponding to that point is recorded, and an ensemble of 200 points is generated. The standard deviation of the bifurcation frequency is obtained by computing the square root of the variance of these frequency points obtained for 200 realizations. In Figure 3.18.a, the standard deviation of the fractional bifurcation frequency in the upper branch (y_u) is plotted versus number of realizations. Next to it, the value of the standard deviation for the same quantity obtained via the non-MC technique is plotted. These values are normalized with the standard deviation obtained via the non-MC technique for generalization. It can be observed that with an increasing number of realizations, the standard deviation values obtained via both methods match each-other. That can be observed better in Figure 3.18.b where the relative error between the two is plotted. As can be seen, the error is continuously decreasing. It is expected that the error decreases even more with a higher number of realizations.

For the backward sweep, the non-MC technique standard deviation is obtained

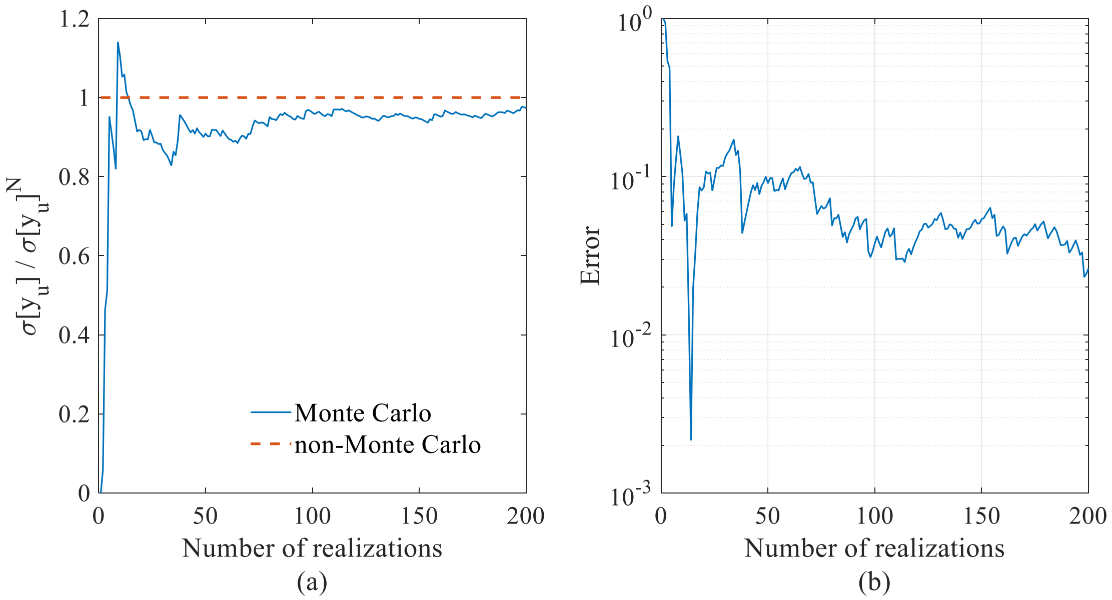

Figure 3.18: Fractional bifurcation frequency standard deviation for the upper branch (y_u) (a) for the Monte Carlo and non-Monte Carlo methods versus number of Monte Carlo realizations, and their error (b)

by using Eqn. (2.64). A_d is defined as the point where the deterministic plot of the output amplitude jumps from the lower branch to the upper branch and is computed in the manner explained in Section 2.3.2. For the MC technique, 200 realizations of the system driven with a backward sweep are obtained. However, obtaining the point where A_d is located for each realization proves to be very challenging in an open-loop sweep setup. We therefore use the deterministic value of A_d obtained via the staircase input as shown in Section 2.3.2, which adds an extra sweep cost to the calculations. For each realization, the point where the output amplitude is equal to the previously obtained A_d value is obtained and the drive frequency corresponding to that point is recorded. An ensemble of 200 frequency points is generated from this data. However, looking at the data obtained by using this exact point, we observe that it does not give reliable results due to its close proximity to the transition between the two branches. Consequently, we performed the same procedure for amplitudes chosen to be slightly further from the transition point to see if a more robust result can be achieved. In Figure 3.19.a we show the variance

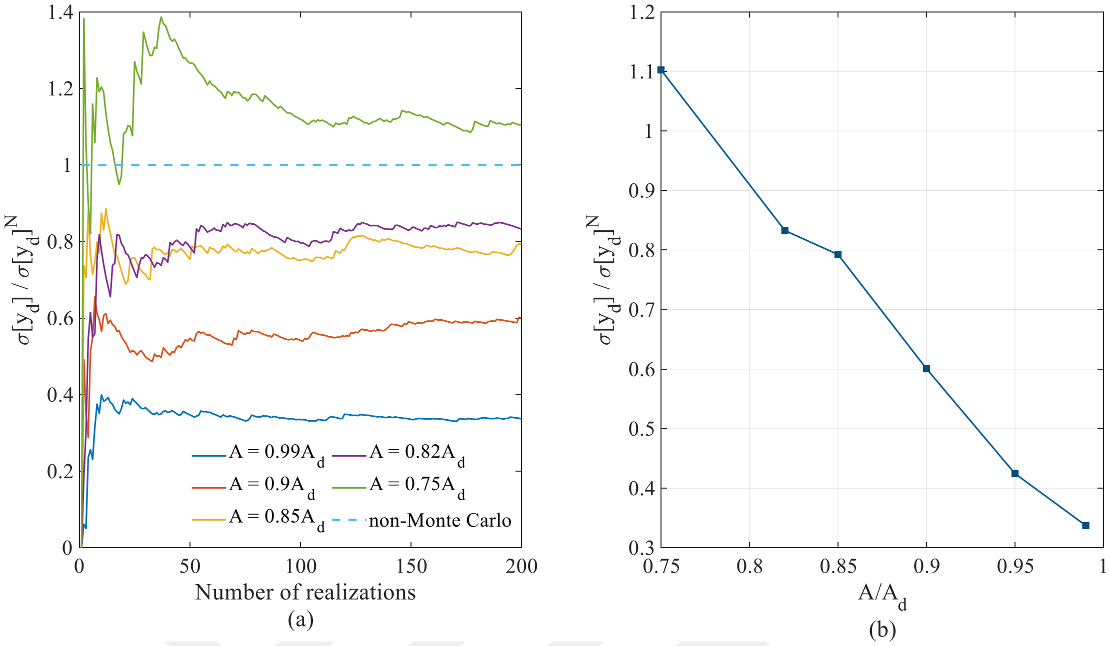

Figure 3.19: (a) Fractional bifurcation frequency standard deviation for the lower branch (y_d) for various selected values A for A_d for the Monte Carlo and non-Monte Carlo methods versus number of Monte Carlo realizations, and (b) the standard deviations obtained for each selected value normalized by the non-Monte Carlo standard deviation for y_d

of y_d versus number of realizations obtained via various points in the vicinity of A_d. The results show that picking the drive frequency at points a bit further from the exact transition point can offer better results than the actual A_d value. In Figure 3.19.b, we can observe how the standard deviation in y_d changes with changes in the selected point. Note that this problem was not present in the y_u standard deviation computation, due to the selected point (A_u) being much more robust and separated from the transition point.

These results point to an inherent problem of the open-loop sweep method for variance computation of the bifurcation frequencies in the nonlinear resonator. The issue lies in the ambiguity of the exact transition point A_d, which leaves the selection of that point in the hands of the user. This is bound to cause some error and decrease the reliability of the use of the open-loop sweep method for f_d variance computation. The same issue is also present in the upper branch, but due to the selected point

A_u being separate from the transition point in a way that can be much more easily detected, it is still much more robust than f_d detection. In contrast, resonance frequency variance computation for the linearly operating resonator proves to be much more reliable. That stems from the fact that it utilizes the variation in phase, where instead of infinite-slope jumps we have a smooth linear function to work with for tracking the resonance frequency.

These results display the weaknesses of the open-loop sweep method, and show that alternative techniques should be sought for more reliable variance computation. One such technique is the trajectory locked loop method proposed in [Yuksel et al., 2019]. In this closed-loop setup, the exact jump points do not have to be selected by the user but are rather chosen automatically by the system itself.

3.3 Method Analysis

3.3.1 Driving the System with Fixed Frequency Input

Both the MC and non-MC technique implementations employ a frequency sweep to obtain the desired variances. The ability to perform this procedure via a frequency sweep is an important advantage of this method, as it warrants variance computation for a dynamic sweep scenario, unlike previous theoretical treatments for the Duffing resonator [Buks and Yurke, 2006] where the system is operating at a fixed point. This enables the experimenter to computationally analyze bifurcation frequency noise under various scenarios, which cannot be investigated under fixed operating point conditions. In cases where the frequency sweep speed is very slow, we can assume that the system is quasi-stationary at each drive frequency, and the variances obtained, especially far from the fast transition points near the bifurcation frequencies, are what we would expect to obtain from a fixed point analysis.

In this section, we investigate whether the results acquired via the quasi-stationary frequency sweeps match the results from fixed drive frequency runs for both the MC and non-MC methods. The MC standard deviations for the system driven with constant frequency are obtained in the following manner. The drive frequency is set to be a constant value. The system is driven at that frequency for a sufficiently

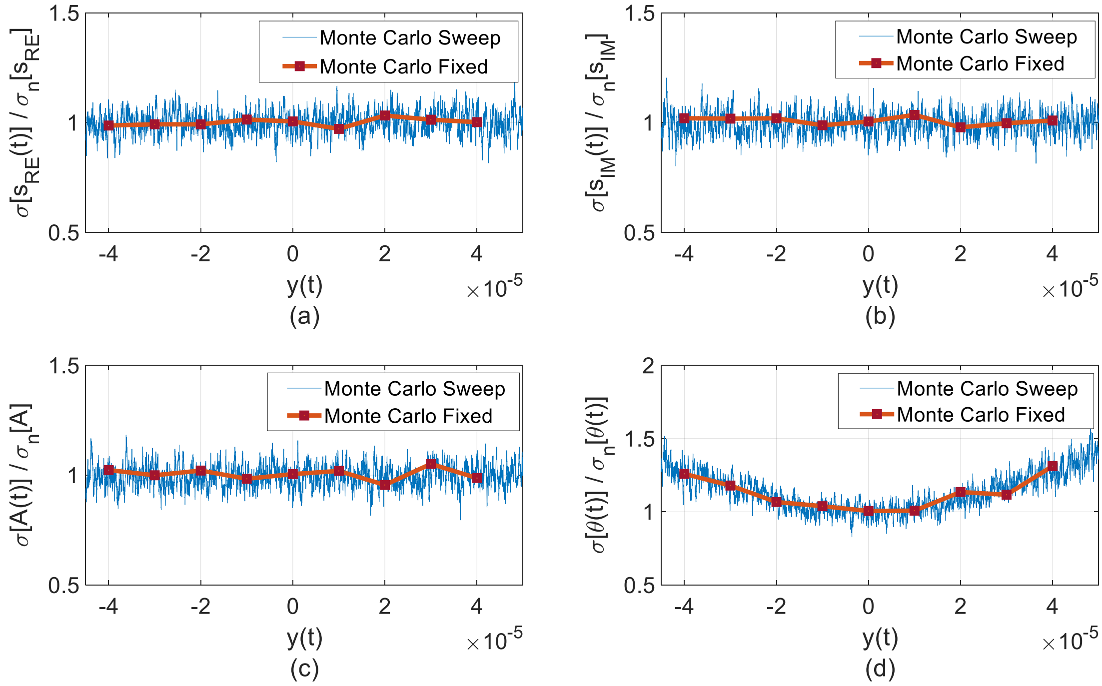

Figure 3.20: Monte Carlo standard deviations of the real part of the output (a), imaginary part (b), amplitude (c) and phase (d) obtained via a frequency sweep, compared with results obtained via fixed frequency simulations of the system operating in the linear regime

long amount of time which permits collecting a meaningful ensemble. The outputs of the system (the real and imaginary parts of the output, the amplitude and the phase) are recorded and as a final step, the standard deviation of the time data is obtained. We note that the initial time data up to 10 times the time constant of the system is removed, so that only steady-state data is used to obtain the time standard deviations. For the non-MC method, the procedure is similar to the frequency sweep simulations, the only difference being that the frequency input is now constant. Note that since the nonlinear system has two stable states, it is important for the constant frequency simulations to first sweep the drive frequency from low to high frequencies up to the desired fixed frequency and then keep the drive frequency constant for the rest of the simulation for f_u computation. The opposite must be done for f_d computation. This ensures that we have the initial conditions which guarantee correct operating points.

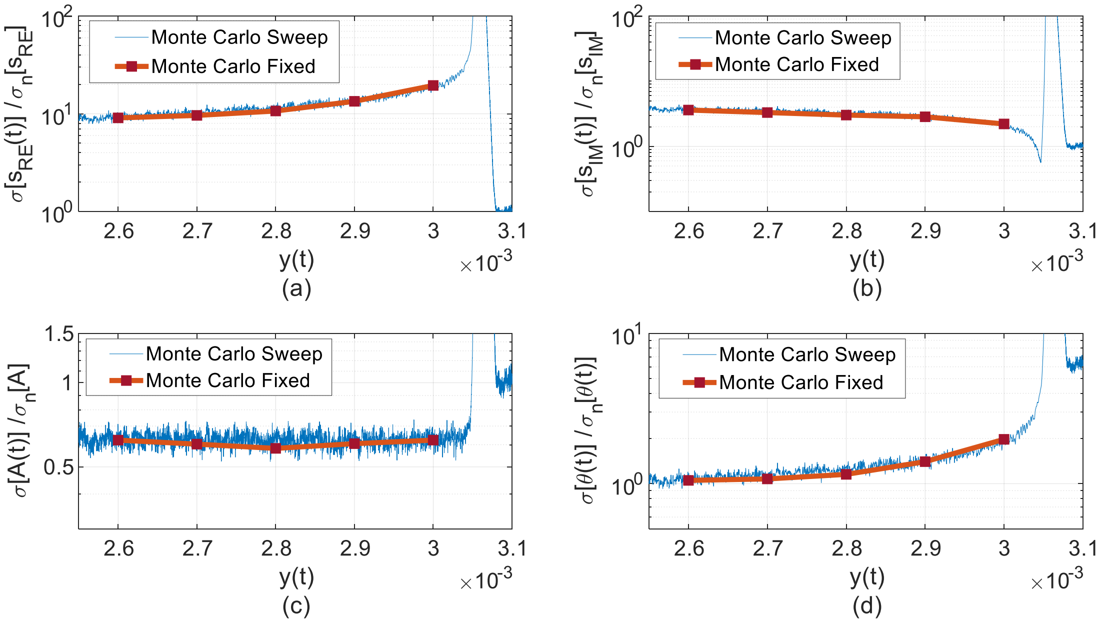

Figure 3.21: Monte Carlo standard deviations of the real part of the output (a), imaginary part (b), amplitude (c) and phase (d) obtained via a forward frequency sweep, compared with results obtained via fixed frequency simulations of the system operating in the nonlinear regime

In Figure 3.20, the normalized MC standard deviations for a frequency sweep around resonance for the linear resonator are compared with data obtained by running the MC system with a constant frequency for various points. As can be observed, the data obtained with a frequency sweep closely matches the data from simulations with a constant frequency drive. Note that the same comparison cannot be done for the resonance frequency standard deviation since its MC computation is different in nature from the computation of the standard deviations in amplitude and phase, and thus cannot be obtained via time averages.

To verify this for the resonator operating in the nonlinear regime, the plots of the normalized standard deviations of the system outputs for the nonlinear system versus those obtained via constant frequency drives are shown in Figure 3.21. The data in Figure 3.21 is obtained via a forward sweep of the frequency. The plots show that the variances acquired from the ensemble of the frequency sweep data are in close agreement with the variances obtained from the time averages from constant

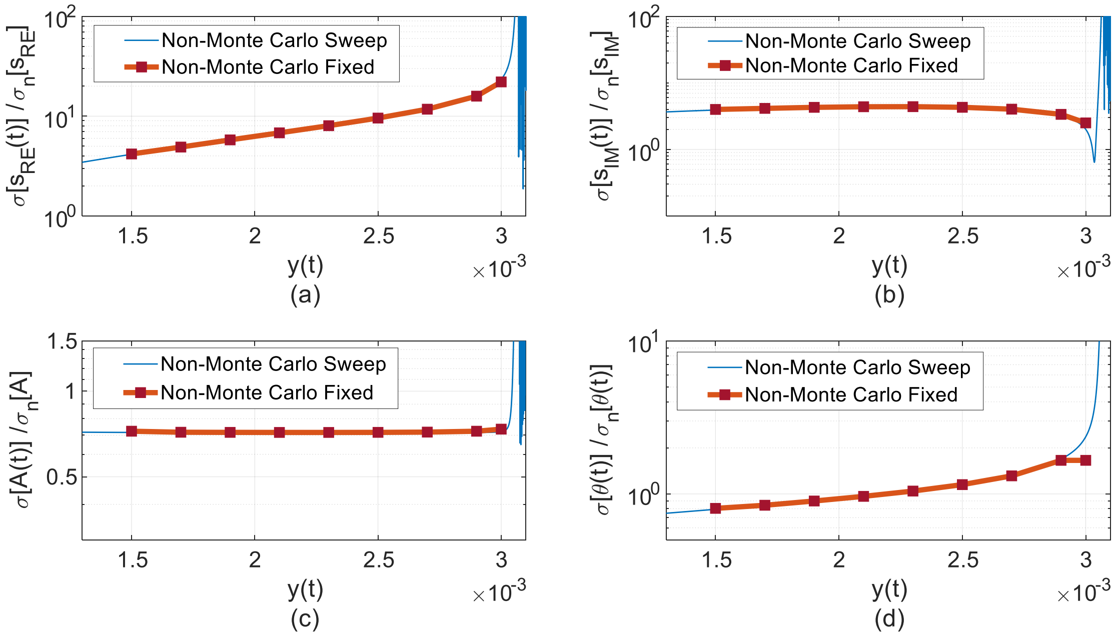

Figure 3.22: Non-Monte Carlo standard deviations of the real part of the output (a), imaginary part (b), amplitude (c) and phase (d) obtained via a forward frequency sweep, compared with results obtained via fixed frequency simulations of the system operating in the nonlinear regime

frequency sweeps.

Next, we investigate whether the same applies to our non-MC technique. We perform a forward sweep of the drive frequency around f_u, and compare these standard deviations with their counterparts obtained via constant frequency inputs. This comparison is shown in Figure 3.22, from which we can deduce that the frequency sweep can produce matching results with the fixed frequency computations.

The results in this section clearly demonstrate that the non-MC technique frequency sweep results are in close agreement with fixed frequency simulation results while being much more efficient, putting in display one of the edges this method has over the fixed frequency techniques.

3.3.2 Analyzing the Effect of Sweep Speed

Since both the MC and non-MC technique implementations use linear sweeps of the drive frequency, we analyze the effect the speed of these sweeps has on the results.

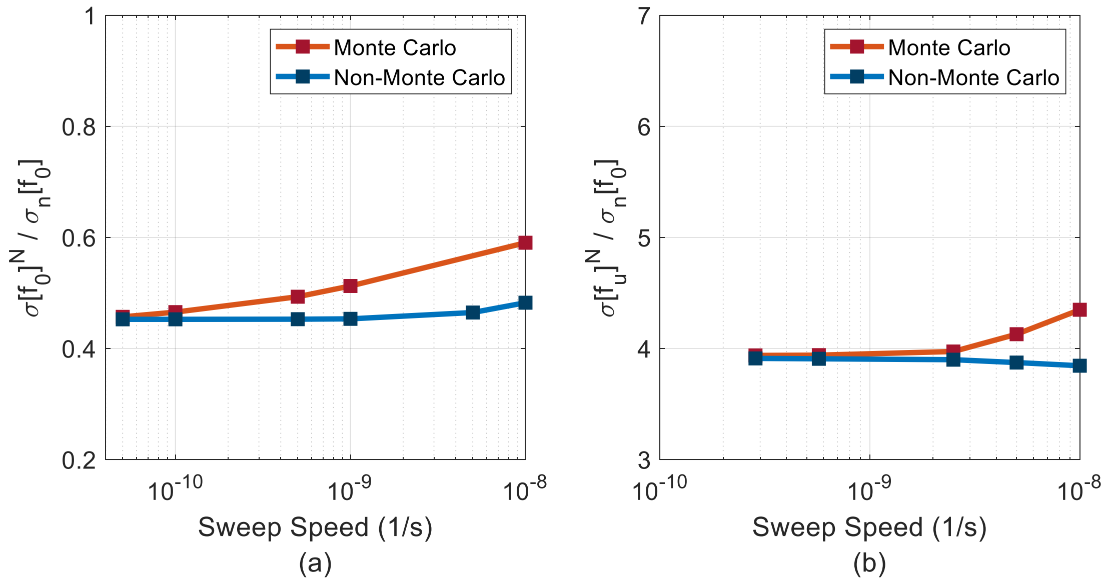

Figure 3.23: Normalized standard deviations for f_o (a) and f_u (b) versus sweep speed obtained via both the Monte Carlo and Non-Monte Carlo techniques

The sweep speed (m) is defined as the fractional frequency deviation swept per unit time (1s), which has a unit of $\frac{1}{s}$.

In Figure 3.23.a, we show a plot of the normalized resonance frequency standard deviations obtained via both methods versus sweep speed. It can be observed that for high sweep speeds, the obtained standard deviations for the resonance frequency value are higher. After decreasing the sweep speed, we can observe that the standard deviations converge to a certain value for which both the MC and non-MC techniques are in agreement. With increasing sweep speed, numerically pinpointing the exact value for the resonance frequency becomes more challenging, which leads to larger errors in standard deviation estimation.

In Figure 3.23.b, we show a plot of the normalized bifurcation frequency standard deviation (of the upper branch) versus sweep speed obtained via both methods. Again, we can observe the importance of the sweep speed in result accuracy. For slower sweep speeds, the MC results agree with the non-MC results. For higher speeds, the MC-obtained standard deviation values begin to deviate further and further, while the non-MC-obtained values begin to dip slightly. This is due to the fact that with a faster sweep, it becomes harder to exactly pinpoint the point where there is a jump in the amplitude, which is the point where the bifurcation frequency is recorded.

These results illustrate that sweep speed is a crucial factor in the accuracy of both the MC and non-MC techniques. However, the non-MC technique fares better with higher sweep speeds compared to the MC method.

Chapter 4

RESULTS

In this section, we use our proposed method to obtain data for various drive amplitudes with the system operating in different regimes. First, we compare these results with experimental data reported in literature. Then, we proceed to make a comparison of the linear and nonlinear regimes and discuss the advantages of one over the other.

4.1 Comparison with Experimental Results

We look into experimental results recently reported in the literature, and see how the results obtained via our method compare with them. The standard deviation values reported in the sections below are all normalized with respect to a selected normalization value $\sigma[y_n]$ for simple comparison. $\sigma[y_n]$ is selected to be the standard deviation of y_o obtained when the system is driven with a magnitude of half the spinodal drive.

4.1.1 Variability of f_u versus f_d

In [Maillet et al., 2018], the presented experimental results indicate that, for the same drive amplitude, the fluctuations in the bifurcation frequency for the upper branch f_u are much larger than the ones in lower branch for f_d. To look into these results, we use our proposed non-MC method to drive the system with different drive amplitudes, and compute the variations $\sigma[y_u]$ and $\sigma[y_d]$. The experiments in [Maillet et al., 2018] are reported to use a drive frequency much further than the spinodal drive D_s. To be consistent, we also chose the drive amplitudes to be at least five times larger than the spinodal drive.

In Figure 4.1.a, the standard deviations of the fractional frequency deviation

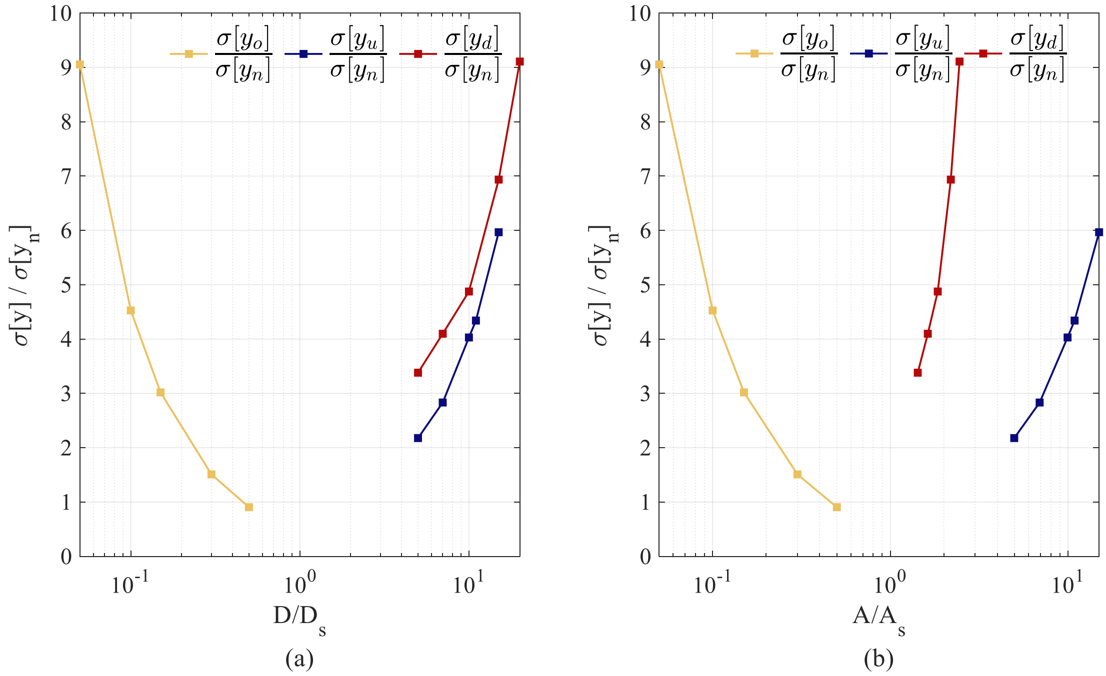

Figure 4.1: $\sigma[y_o]$, $\sigma[y_u]$ and $\sigma[y_d]$ versus normalized drive amplitude (a) and $\sigma[y_o]$, $\sigma[y_u]$ and $\sigma[y_d]$ versus normalized motion amplitude (b)

values for both the upper and lower branches versus normalized drive amplitude are plotted. It can be observed that for the same drive amplitude (normalized by the spinodal drive amplitude D_s), differently from the experimental results, the variation in $\sigma[y_d]$ is actually larger than the fluctuations in $\sigma[y_u]$.

4.1.2 Variability of f_u and f_d versus Motion Amplitude

The results in Section 4.1.1 show that for the same drive amplitude, the variation of $\sigma[y_d]$ surpasses that of $\sigma[y_u]$. In those circumstances, due to the nature of the system, the motion amplitude for the upper branch A_u is much higher than the motion amplitude of the lower branch A_d. We now analyze what happens when we compare the fluctuations in the bifurcation frequencies of both branches versus motion amplitude.

In Figure 4.1.b, the standard deviations of the fractional frequency deviation values for both the upper and lower branches versus normalized motion amplitude

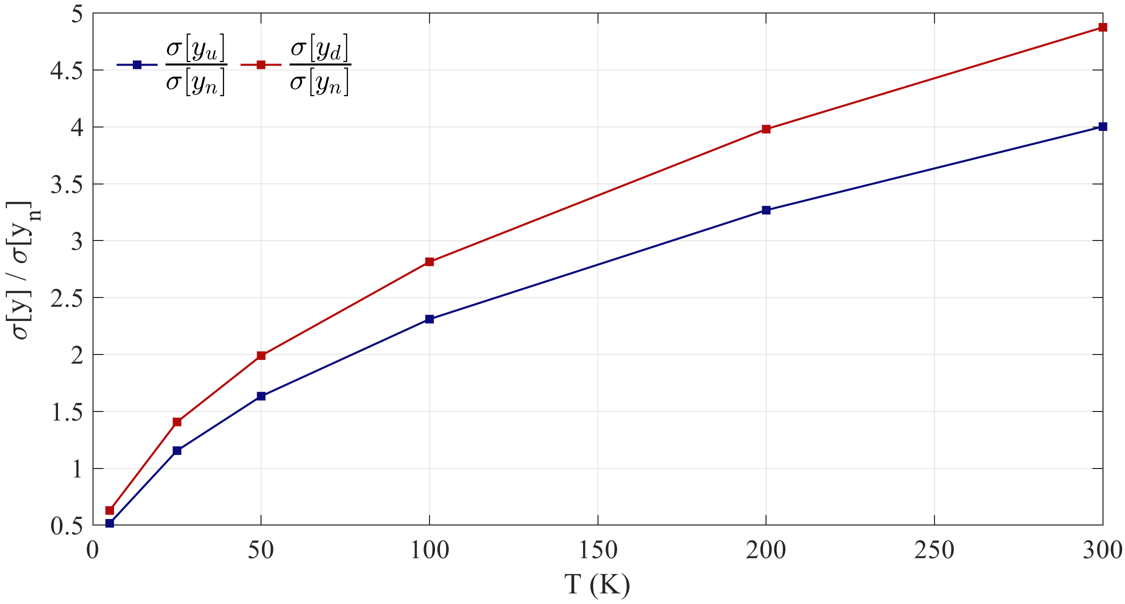

Figure 4.2: Temperature dependence of $\sigma[y_u]$ and $\sigma[y_d]$

are plotted. The plot shows that now the difference between the two variations is even greater. Since $\sigma[y_d]$ is greater than $\sigma[y_u]$ for the same drive amplitude and the variations keep increasing with drive amplitude, it is expected that for the same motion amplitude the difference be even larger, which is the case. This difference is further amplified by the expressions in Eqns. (2.63) and (2.64), where the variance of f_d is shown to have an extra scaling of 9 compared to that of f_u due to their different relationship with motion amplitude. These results lead us to conclude that using the variation in f_u provides more accurate results than using f_d.

4.1.3 Variability of f_u and f_d versus Temperature

The temperature dependence of bifurcation frequency standard deviations is considered in this section. The system with identical parameters is driven with the same drive amplitude for various temperature values, and bifurcation frequency standard deviations versus temperature for both the upper and lower branches are obtained and shown in Figure 4.2. We observe that the standard deviation scales with the square root of temperature meaning that the variance depends linearly on it, in accordance with the experimental results in [Maillet et al., 2018], and as expected since the source of variability is thermomechanical fluctuations.

4.2 Variability in the Linear and Nonlinear Regimes

In this section, we compare the variability in frequency of a resonator in the linear and nonlinear operating regimes. As shown in Figure 4.1.a, for the linear regime, the resonance frequency variability diminishes with increasing drive amplitude. As a result, better performance can be achieved in this regime by driving the system with greater drive amplitudes. However, increasing the drive amplitude to levels near and beyond the spinodal point pushes the resonator into the nonlinear regime, where the system dynamics change and resonance frequency tracking is no longer possible [Maillet et al., 2018], [Yuksel et al., 2019].

In the nonlinear oscillations regime, nonlinear mixing causes the additive noise to be enhanced which results in more pronounced frequency variability for greater drive amplitudes. In this scenario, the drive amplitude should be as small as possible in order to minimize variability in the bifurcation frequencies. However, similar to the case in the linear regime, operating near the spinodal point this time pushes the system back to the linear operating regime, where the hysteretic behavior and hence the bifurcation frequencies are no longer observable. As a result, operating in the desired regime and at an optimal drive level should be achieved by a careful selection of the drive amplitude.

In Figure 4.1, the normalized standard deviation values of the three fractional frequencies of interest at various distances from the spinodal point are shown. As can be observed, the variations in the nonlinear regime are not very far off from the variations in the linear regime. Although the linear system performs better for amplitudes close to the spinodal point, it can be argued that since a drive amplitude large enough to keep the system in the desired operating region is needed, both systems offer similar performance. However, the nonlinear operating point, with its larger motion amplitude, offers better dynamic range when transduction (detection) noise is not negligible.

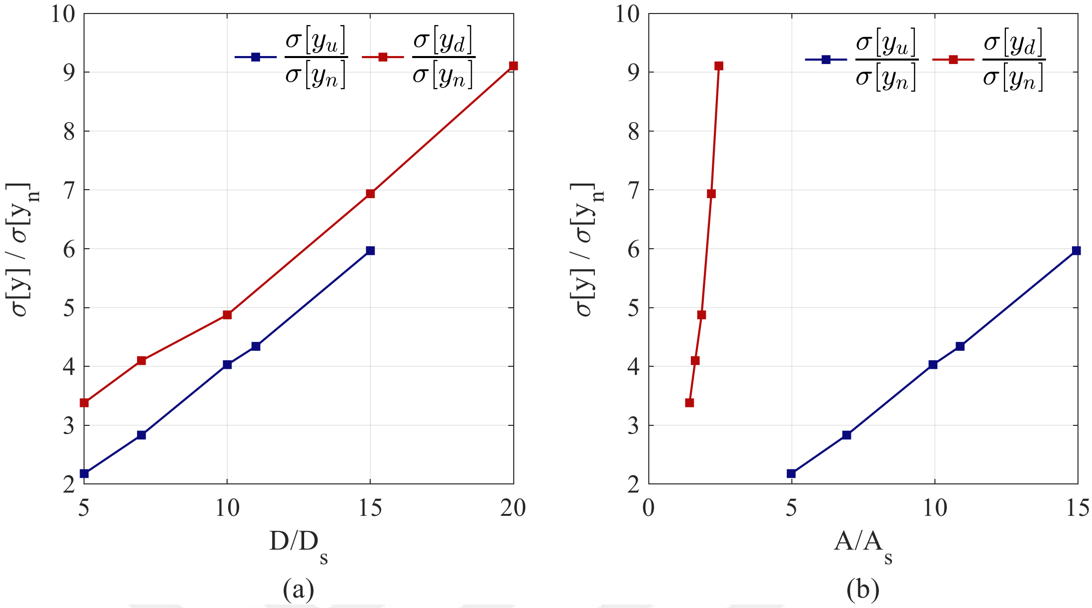

Figure 4.3: $\sigma[y_u]$ and $\sigma[y_d]$ versus normalized drive amplitude (a) and $\sigma[y_u]$ and $\sigma[y_d]$ versus normalized motion amplitude (b)

Experimental results from open-loop sweeps reported in [Maillet et al., 2018] show a quadratic relationship between the standard deviation of the bifurcation frequency and the motion amplitude. We use the proposed computational method to generate the data in Figure 4.3.b, where the relationship between the fractional bifurcation frequency standard deviations and motion amplitude is plotted for both the upper and lower branches, *i.e.*, normalized y_u and y_d. These results show that the standard deviation is linearly dependent on motion amplitude, in contrast with the experimental results reported in [Maillet et al., 2018] which show a quadratic dependence. Based on the analytical underpinnings of our method, we can in fact argue the sensibility of the results we have obtained as follows. For a linear resonator, it can be easily shown that the resonance frequency standard deviation has an inverse dependence on motion amplitude. The reason for this is rooted in the conversion of additive noise into phase/frequency noise via scaling with inverse amplitude [Demir and Hanay, 2020]. In the nonlinear Duffing regime, the mixing of additive noise with the signal through the cubic nonlinearity produces a dominant, additive noise term that is proportional to the square of the motion amplitude. This noise term, when mapped to frequency noise, is scaled with inverse amplitude, yielding an overall linear scaling with amplitude. Thus, within the scope of our model, it is inexplicable that the experimental results in [Maillet et al., 2018] translate to a *quadratic* scaling in the standard deviation *w.r.t.* motion amplitude. A possible reason for this discrepancy might be the fact that our method only models thermomechanical noise, while the source of this variability could be due to some other phenomenon or property of the system not modeled here.

The results presented in this section indicate that the resonator in the nonlinear operating regime can be a valid alternative to the linearly operating resonator in terms of sensing performance. The results also point that, if used, best sensing performance with the nonlinear resonator can be achieved by using the bifurcation frequency of the upper branch f_u, which displays less variation. This argument is strengthened by the lack of robustness of f_d computation for an open-loop sweep setup (as discussed in Section 3.2.2). The proposed computational technique can be used to both confirm but also challenge experimentally obtained characterizations, as well as in the conception of new experimental scenarios.

Chapter 5

SUMMARY AND CONCLUSION

This thesis presents two main contributions:

i The repurposing of a semi-analytical, efficient, non-Monte Carlo numerical characterization technique, originally developed for noise characterization in analog circuits, to examine the variability in the bifurcation frequencies in the nonlinear Duffing resonator due to thermomechanical noise. The non-Monte Carlo technique is in agreement with computationally expensive Monte Carlo simulations, while drastically improving computation time. Apart from replacing brute force Monte Carlo simulations, the proposed method presents the advantage of a dynamic characterization. The bifurcation frequency variability can be obtained dynamically while the input frequency is changing. This paves the way for a more rigorous analysis of the behavior of the nonlinear Duffing resonator, adding to the number of scenarios that can be analyzed under sweep-like conditions, as is in fact the case when we are trying to assess the performance of the system in a setup such as that in the open-loop sweep experiments in [Maillet et al., 2018]. This is one of the advantages this technique has over the fixed-frequency characterizations such as that in [Buks and Yurke, 2006]. This technique is not limited to the model of the Duffing resonator. It can also be generalized for use in various nonlinear resonator models and closed-loop setups.

ii The application of the non-Monte Carlo technique for analyzing the performance of the open-loop sweep method for bifurcation frequency noise characterization, similar to the experiments in [Maillet et al., 2018]. The analysis reveals that due to its nature, the open-loop sweep method is not very reliable for employment in bifurcation frequency noise characterizations and as a sensing scheme in the nonlinear regime, in contrast to the linear regime, where it proves to be very robust. These results confirm the observations stated in [Yuksel et al., 2019] regarding open-loop nonlinear sensing schemes. If, however, the use of a nonlinear resonator in an open or closed-loop configuration is necessary, then the results point to the upper branch bifurcation frequency as the more reliable option, due to its lower variation and more reliable detection.

In Chapter 1 we provide a brief background on oscillatory systems and their behavior in the linear and nonlinear oscillation regimes.

In Chapter 2 we delve into the theory behind the proposed technique. We first introduce the Duffing resonator model and its baseband equivalent. This formulation offers the advantage of operating at low frequencies, which decreases the computation time while still retaining all information regarding the phenomena of interest. Then we introduce the non-Monte Carlo method for characterizing the frequency fluctuations in the Duffing resonator, which drastically improves computational efficiency due to the fact that it does not require multiple sweeps to form a statistical ensemble, unlike experimental and Monte Carlo based computational techniques.

In Chapter 3, we validate the approximations employed in the non-Monte Carlo technique. We first validate the deterministic and stochastic baseband equivalent model by comparing its results with those of the passband system. Then, we proceed to investigate the accuracy of the non-Monte Carlo technique via extensive Monte Carlo simulations, confirming that our proposed method is indeed in agreement with the Monte Carlo data. The results in the comparison data expose some of the limitations of the open-loop sweep characterization technique.

In Chapter 4, we compare the results of the proposed technique against experimental results presented in literature. Then we proceed to use the proposed non-Monte Carlo technique to assess the performance of the Duffing resonator in the nonlinear regime as opposed to its performance in the linear regime. From the results, we establish that optimal sensitivity and a large dynamic range in the presence of detection noise may be attained by operating a nonlinear resonator at a point that is close to the spinodal point.

Due to its computational efficiency, this method may be used in exploring fundamental sensitivity limits of nonlinear resonator based sensors. It will be a valuable tool for researchers in the nanomechanical sensors field that can help decipher noise phenomena in the system and conceive the best design for a specific purpose, before conducting expensive and time-consuming experiments. Future work includes extending this technique for the characterization of novel closed-loop systems based on nonlinear resonators, such as the one proposed in [Yuksel et al., 2019]. This technique, known as the trajectory-locked loop (TLL) differs from the powerful phase-locked loop (PLL) technique for linear resonators in that instead of locking the sensor at a single phase, it traps the system inside the hysteresis window, where the system is locked in a trajectory that spans the two bifurcation frequencies, which are employed for detection. This technique is expected to fare better than the open-loop sweep technique in bifurcation frequency noise characterizations and as a sensing scheme.

BIBLIOGRAPHY

[Benedetto and Biglieri, 1999] Benedetto, S. and Biglieri, E. (1999). *Principles of Digital Transmission: with Wireless Applications*. Springer Science & Business Media.

[Buks and Yurke, 2006] Buks, E. and Yurke, B. (2006). Mass detection with a nonlinear nanomechanical resonator. *Physical Review E*, 74(4):046619.

[Chaste et al., 2012] Chaste, J., Eichler, A., Moser, J., Ceballos, G., Rurali, R., and Bachtold, A. (2012). A nanomechanical mass sensor with yoctogram resolution. *Nature Nanotechnology*, 7(5):301–304.

[Demir, 2021] Demir, A. (2021). Understanding fundamental trade-offs in nanomechanical resonant sensors. *Journal of Applied Physics*, 129(4):044503.

[Demir and Hanay, 2018] Demir, A. and Hanay, M. S. (2018). Numerical analysis of multi-domain systems: Coupled nonlinear PDEs & DAEs with noise. *IEEE Transactions on Computer-Aided Design of Integrated Circuits & Systems*, 37(7):1445–1458.

[Demir and Hanay, 2020] Demir, A. and Hanay, M. S. (2020). Fundamental sensitivity limitations of nanomechanical resonant sensors due to thermomechanical noise. *IEEE Sensors Journal*, 20(4):1947–1961.

[Demir and Sangiovanni-Vincentelli, 1998] Demir, A. and Sangiovanni-Vincentelli, A. (1998). *Analysis and Simulation of Noise in Nonlinear Electronic Circuits and Systems*. Springer.

[Ekinci et al., 2004] Ekinci, K., Yang, Y., and Roukes, M. (2004). Ultimate limits to inertial mass sensing based upon nanoelectromechanical systems. *Journal of Applied Physics*, 95(5):2682–2689.

[Greywall et al., 1994] Greywall, D. S., Yurke, B., Busch, P. A., Pargellis, A. N., and Willett, R. L. (1994). Evading amplifier noise in nonlinear oscillators. *Physical Review Letters*, 72:2992–2995.

[Hanay et al., 2012] Hanay, M., Kelber, S., Naik, A., Chi, D., Hentz, S., Bullard, E., Colinet, E., Duraffourg, L., and Roukes, M. (2012). Single-protein nanomechanical mass spectrometry in real time. *Nature Nanotechnology*, 7(9):602–608.

[Kenig et al., 2012] Kenig, E., Cross, M. C., Villanueva, L. G., Karabalin, R. B., Matheny, M. H., Lifshitz, R., and Roukes, M. L. (2012). Optimal operating points of oscillators using nonlinear resonators. *Physical Review E*, 86(5):056207.

[Landau and Lifshitz, 1976] Landau, L. D. and Lifshitz, E. M. (1976). *Mechanics*, volume 49. Elsevier.

[Lifshitz and Cross, 2008] Lifshitz, R. and Cross, M. (2008). Nonlinear dynamics of nanomechanical and micromechanical resonators. *Reviews of Nonlinear Dynamics and Complexity*, pages 1–52.

[Maillet et al., 2018] Maillet, O., Zhou, X., Gazizulin, R. R., Ilic, R., Parpia, J. M., Bourgeois, O., Fefferman, A. D., and Collin, E. (2018). Measuring frequency fluctuations in nonlinear nanomechanical resonators. *ACS Nano*, 12(6):5753–5760.

[Süli and Mayers, 2003] Süli, E. and Mayers, D. F. (2003). *An Introduction to Numerical Analysis*. Cambridge University Press.

[The MathWorks, Inc., 2020] The MathWorks, Inc. (2020). MATLAB® Simulink®.

[Yuksel et al., 2019] Yuksel, M., Orhan, E., Yanik, C., Ari, A. B., Demir, A., and Hanay, M. S. (2019). Nonlinear nanomechanical mass spectrometry at the single-nanoparticle level. *Nano Letters*, 19(6):3583–3589.

[Yurke et al., 1995] Yurke, B., Greywall, D. S., Pargellis, A. N., and Busch, P. A. (1995). Theory of amplifier-noise evasion in an oscillator employing a nonlinear resonator. *Physical Review A*, 51:4211–4229.